analytical chemistry

pubs.acs.org/ac Article

A Fluorogenic Pseudoinfection Assay to Probe Transfer and Distribution of Influenza Viral Contents to Target Vesicles

Ahanjit Bhattacharya, Nahal Bagheri, and Steven G. Boxer*

Cite This: *Anal. Chem.* 2024, 96, 13033−13041 Read Online

ACCESS | Metrics & More | Article Recommendations | Supporting Information

ABSTRACT: Fusion of enveloped viruses with endosomal membranes and subsequent release of the viral genome into the cytoplasm are crucial to the viral infection cycle. It is often modeled by performing fusion between virus particles and target lipid vesicles. We utilized fluorescence microscopy to characterize the kinetic aspects of the transfer of influenza viral ribonucleoprotein (vRNP) complexes to target vesicles and their spatial distribution within the fused volumes to gain deeper insight into the mechanistic aspects of endosomal escape. The fluorogenic RNA-binding dye QuantiFluor (Promega) was found to be well-suited for direct and sensitive microscopic observation of vRNPs which facilitated background-free detection and kinetic analysis of fusion events on a single particle level. To determine the extent to which the viral contents are transferred to the target vesicles through the fusion pore, we carried out virus-vesicle fusion in a side-by-side fashion. Measurement of the Euclidean distances between the centroids of superlocalized membrane and content dye signals within the fused volumes allowed determination of any symmetry (or the lack thereof) between them as expected in the event of transfer (or the lack thereof) of vRNPs, respectively. We found that, in the case of fusion between viruses and 100 nm target vesicles, ∼39% of the events led to transfer of viral contents to the target vesicles. This methodology provides a rapid, generic, and cell-free way to assess the inhibitory effects of antiviral drugs and therapeutics on the endosomal escape behavior of enveloped viruses.

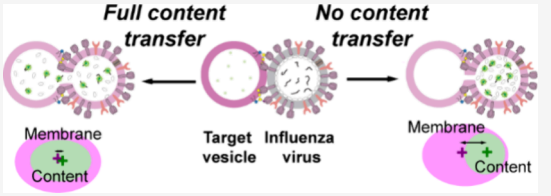

INTRODUCTION

There is a long-standing interest in studying viral fusion from a biophysical perspective to dissect the underlying interplay between proteins and lipids involved in the process.[1,2] In a bottom-up biophysical model, one can precisely control the composition of the system to ascertain which components are essential to a process and quantify their molecular contributions. Fusion of virus particles with lipid vesicles, sometimes referred to as pseudoinfection, is a commonly described model of viral cellular entry under controlled conditions (pH, temperature, time, target membrane composition and curvature).[3,4] Since viral membrane fusion is an inherently heterogeneous process, observation of a large number of such events on a single particle level can reveal pathways and mechanistic details that may remain obscure in ensemble studies.[5] Until now, diffraction-limited fluorescence microscopy and cryogenic transmission electron microscopy (cryo-TEM) have been the preferred methods for studying viral fusion on a single-particle level.[3] While fluorescence microscopy provides information about fusion kinetics, cryo-TEM provides a direct visualization of the fusion intermediates over a population.

Influenza virus is a widely studied pathogen as the causative agent of seasonal epidemics and occasional but unpredictable pandemics. It is a canonical enveloped virus that delivers its macromolecular contents to the host cell via membrane fusion. The lipid envelopes of the influenza virus particles are decorated with hundreds of copies of the glycoprotein hemagglutinin (HA) which is necessary for attachment of the virus particles to cell surface sialic acid receptors (Figure 1A).[6] The influenza viral genome consists of eight single-stranded, negative sense RNA segments organized into macromolecular assemblies called viral ribonucleoproteins (vRNPs).[7] Electron microscopy studies have revealed that vRNPs are double helical structures 30−120 nm in length.[8] Within the vRNPs, the RNA strand is bound to the nucleoprotein (NP) scaffold by interaction with its phosphodiester backbone such that, on average, there is 1 NP per 24 ribonucleotides.[9] Inside the virus particles, the vRNPs associate with the matrix protein (M1) layer.[10] Following binding to the cell surface receptors, the virus particles are endocytosed within the endosomes. When the pH inside the endosome drops below 5.5, HA undergoes conformational change, which triggers fusion between viral and endosomal membranes. Also, M2 channels pump protons to the viral interior leading to dissociation of the M1 layer from the viral membrane which in turn becomes more amenable to fusion.[11] At the same time, the interaction between the M1 proteins and vRNPs weakens and the latter are released into the cytoplasm via

Received: February 29, 2024
Revised: July 17, 2024
Accepted: July 17, 2024
Published: August 1, 2024

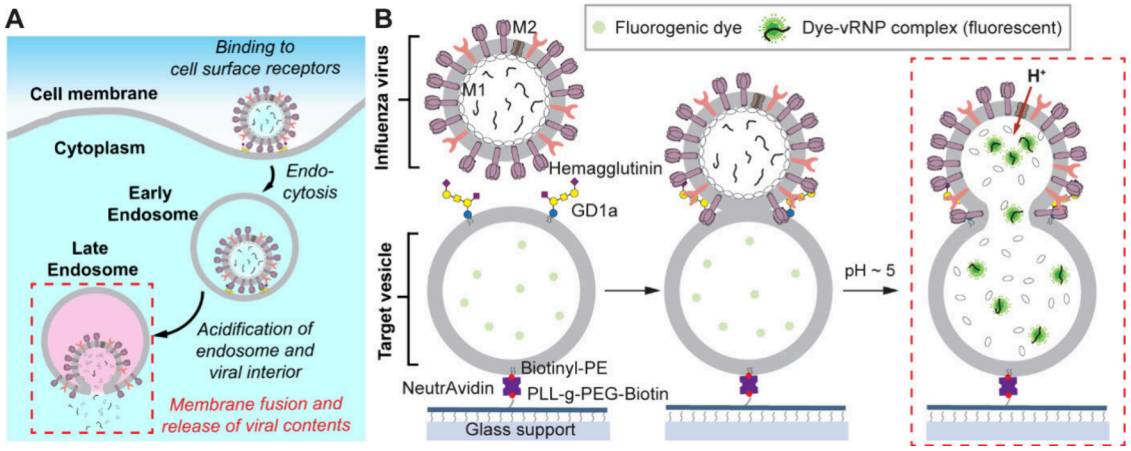

Figure 1. Pseudoinfection model of viral cellular entry. (A) Schematic representation of the steps leading to the cellular entry of the influenza virus. Fusion of a virus particle with an endosomal membrane is triggered by acidification of endosomes. (B) Schematic representation of the fusion of influenza virus particles with target vesicles tethered to a glass surface. The virus particles bind to the target vesicles via sialic acid-containing lipid (GD1a) receptors (two molecules shown for simplicity). Fusion is triggered by a drop in pH. Upon opening of the fusion pore, the nucleic acid-binding dye molecules come into contact with the viral ribonucleoprotein (vRNP) complexes and turn on fluorescence. This step is marked with a dashed rectangular box to highlight the analogy with endosomal membrane fusion depicted in part A.

a fusion pore, a process known as endosomal escape (Figure 1A).[12]

The pseudoinfection model recapitulates two fundamental steps of the endosomal escape process, mixing of lipid compartments and transfer of viral contents (Figure 1B).[3] While lipid mixing between virus and vesicle membranes is a rapid way to test that the viral fusion protein is functional,[13] many such events are halted at the intermediate hemifused state where the outer leaflets of the two membranes merge but not the inner leaflets, and consequently, no fusion pore is formed.[14] On the other hand, a content mixing experiment provides more information, namely, the presence of a functional fusion protein, formation of a fusion pore, and possible presence of the viral genome, though the fusion pore may not necessarily be large enough to accommodate passage of the vRNPs (viral genome).

To observe content mixing between virus and vesicle compartments, typically, a water-soluble dye is encapsulated at self-quenching concentration within the virus or target vesicle interior whose fluorescence is enhanced due to dilution upon fusion.[15−17] These assays have been popular because content label dyes such as calcein and sulforhodamine B (SRB) are relatively inexpensive (an important practical consideration since only a small fraction of dye gets encapsulated during preparation of the target vesicles). However, they suffer from a few drawbacks. First, a very high concentration (tens of millimolar) of the content label dye needs to be encapsulated in the target vesicle lumen. Dyes like SRB can strongly associate with lipid membranes,[18] and therefore, it can be expected that such dyes may perturb the mechanical properties of the target vesicle membranes and therefore influence the fusion behavior. Second, content loss events due to vesicle bursting complicate the analysis of these assays.[16] Finally, content mixing assays based on the dequenching of soluble dyes have to rely on indirect evidence and do not detect the viral macromolecular content (genome) directly. Therefore, a probe that enables direct visualization of viral RNA in infectious particles without potentially perturbing the target vesicle membranes would be highly desirable.

Fluorescence In Situ Hybridization (FISH) probes have been used to detect specific viral sequences in fixed and permeabilized viral preparations.[19] However, such probes are not fluorogenic and need wash steps which limits their applicability for real-time tracking studies. Molecular beacons are fluorogenic oligonucleotide probes which turn on in fluorescence upon hybridizing with target nucleic acid sequences. However, it is not obvious whether the complementary sites on the viral RNA will be accessible to such probes since the viral RNA typically remains bound to proteins. Moreover, to encapsulate even a few (<10) copies of molecular beacons inside target vesicles (∼100 nm in diameter), one needs to start with at least tens of micromolars of the probe in the hydration solution which may pose practical challenges such as high cost. Simple nucleic acid-binding fluorogenic dyes may be advantageous in situations where detection of any viral nucleic acid is desirable. In this work, we systematically screened many commercially available nucleic-acid binding dyes to evaluate the feasibility of their use in microscopy-based viral content transfer experiments as illustrated in Figure 1B. The RNA-binding dye QuantiFluor offered the most optimal physicochemical (brightness and photostability) characteristics for this experiment. Using fluorescence microscopy, we probed the kinetic aspects of virus-vesicle fusion events on a single particle level. Using superlocalization microscopy and a novel fusion geometry introduced later, we probed the pattern of distribution of viral contents within the fused volume to determine the efficiency of content transfer through the fusion pore. Taken together, we show that our method is applicable for semiquantitative estimation of viral infectivity and efficiency of endosomal escape in a straightforward, cell-free manner.

EXPERIMENTAL SECTION

Compositions of *vesicle buffer*, *fusion buffer*, and *lysis buffer* are provided in the Supporting Information and Methods.

Content Transfer Assay (Figures 1B and 2). *Experimental Setup.* In a freshly prepared microfluidic flow cell (Figure S3), the channels (glass surfaces) were passivated with 20:1 PLL-*g*-PEG/PLL-*g*-biotin-PEG. The vesicles encapsulating QuantiFluor (or another nucleic acid-binding dye) were tethered with the passivated glass surface via NeutrAvidin. Excess vesicles were removed by rinsing the channel with *vesicle*

https://doi.org/10.1021/acs.analchem.4c01142
Anal. Chem. 2024, 96, 13033−13041

buffer. Next, virus particles were added to the flow cell and allowed to bind to the vesicles for ∼10 min. Unbound virus particles were removed by rinsing the channel with *vesicle buffer*. pH was dropped by flowing in *fusion buffer* while a continuous video stream was acquired (SI Video 1). The wait time between lowering of pH and appearance of a bright spot (fusion event) were calculated using custom-written MATLAB scripts. The wait times were plotted into cumulative distribution functions (CDFs). To rule out the possibility that turn on events were caused by passive diffusion of QuantiFluor released from any ruptured target vesicle into a ruptured virus particle, an appropriate control experiment was done as described in Supporting Information and Methods ("Control experiments for content transfer assay" and SI Video 2).

Superlocalization Experiments (Figures 3−5). The details of preparation and characterization of gel phase SLBs are provided in the Supporting Information and Methods.

Virus-Vesicle Fusion and Imaging. After tethering the vesicles and then the viruses according to the scheme outlined in Figure 5A, images were taken in 561 nm (*magenta*) and 488 nm (*green*) channels at various contiguous nonoverlapping locations of the imaging slide. No spots were detected in the *green* channel images. The pH was dropped by flowing the sample in *fusion buffer*. After 30 min, two channel images were taken at the same positions as those previously. In the *green* (QuantiFluor-RNA) channel, new fluorescent spots could be seen overlapping with *magenta* (membrane) spots corresponding to each fusion event. The 30 min delay was chosen based on previous cryo-ET studies, showing that this is long enough for the fusion structures to reach their final morphologies.[11,20,21] For nucleozin experiments, the virus particles labeled with appropriate DNA-lipid conjugates were incubated in *vesicle buffer* containing 100 μM nucleozin for 1 h at RT.

Chromatic Aberration Correction. Chromatic aberration correction was carried out using the FIJI plugin Detection of Molecules (DoM) version 1.2.4. TetraSpeck beads (Thermo Fisher) were used for channel registration. One μL of the 100 nm bead dispersion was diluted to 100 μL with Milli-Q water and put in a bath sonicator for 1 h. A fresh microfluidic flow cell (Figure S3) was prepared and functionalized with PLL−PEG. Ten μL of the bead dispersion was added and adsorbed for >10 min. Excess beads were rinsed away. Image stacks were taken consecutively in 488 nm (*green*) and 561 nm (*magenta*) channels with exposure and illumination settings such that pixel intensity values of $\sim 10^4$ were obtained at the center of a particle. Next, the chromatic calibration table containing the displacement vectors across the FOV was calculated. This table was used to correct for the images taken in the *magenta* channel.

ThunderSTORM analysis. The FIJI plugin ThunderSTORM (Version 1.3)[22] was used to superlocalize the signals from individual diffraction limited particles (fluorescent beads, vesicles, or virus-vesicle fused volumes). A B-Spline wavelet filter (order = 3, scale = 2.0) was used to filter the images. A local maximum algorithm was used to approximate the localization of particles with 2 × std peak intensity threshold (2.0 × std(Wave.F1)) and 8-neighborhood connectivity. The point spread function was fitted by a weighted least-squares method using a 7-pixel fitting radius and initial sigma of 1.6 pixel. The superlocalized centroids of particles were corrected for chromatic aberration using DoM plugin as applicable. Euclidean distance between two superlocalized points in magenta (x_M, y_M) and green channels (x_G, y_G) is defined as $d_{MG} = \sqrt{(y_M - y_G)^2 + (x_M - x_G)^2}$, and they were calculated using the "Colocalization" menu. Superlocalized coordinates were filtered on the basis of predefined "sigma" and "uncertainty" values which were kept constant for all comparative analyses to deduce meaningful comparisons between d_{MG} distributions.

RESULTS AND DISCUSSION

Selection of a Suitable Nucleic Acid-Binding Dye for Content Transfer Experiments. Initially, we screened the dyes suitable for the content transfer assay (Table S1, Figure S1) based on the following criteria: (i) good aqueous solubility to achieve sufficiently high encapsulated dye concentration within vesicles; (ii) fluorescence properties not significantly altered between pH 7.5 and 5; (iii) impermeability to lipid membranes; (iv) minimal binding to lipid membranes;[18] (v) efficient binding to vRNPs leading to high signal above background when bound to viral RNA; and (vi) photostability. In a typical screening experiment, 100 nm unilamellar vesicles (ULVs) encapsulating a particular dye were tethered to a passivated glass surface and fusion with influenza virus was triggered by flowing in pH 5.1 buffer (Figure 1B). Bright spots were generated against minimal background, indicating that a given dye bound to vRNPs following membrane fusion (Figure S4). Among all dyes tested, we observed that the RNA-specific dye QuantiFluor (Promega) offered the best combination of properties necessary for the detection of viral contents (Figure S5A−E for dye characterization). We further tested the binding of QuantiFluor with vRNPs present in a detergent-lysed virus sample and found that the fluorescence of QuantiFluor was significantly turned on in the viral lysate (Figure S5F). The fluorescence was practically unchanged when the lysate was digested with proteinase K suggesting that NPs do not hinder binding of QuantiFluor to the viral RNA. A few members of the SYBR family of dyes also showed fluorescence turn on in the microscopy assay, but they presented some limitations. The signals from SYBR Green I and SYBR Green II diminished rapidly under the standard imaging conditions due to photobleaching (Figure S6). The signal from SYBR Gold was relatively stable; however, the level of the signal above the background was significantly weaker as compared to QuantiFluor (Figure S6). SYBR Safe, a dye used in gel staining, did not lead to any fluorescence turn on. We found the bis-intercalating dye DiYO-1 was suitable for the content transfer assay, consistent with the results described previously in an influenza viral genome exposure assay.[17] We further observed that DiYO-1 produced a stable signal under our imaging conditions (Figure S6), albeit we had to use a starting dye concentration of 100 μM to encapsulate sufficient dye molecules inside target vesicles to achieve appreciable signal levels compared to 10 μM described by the previous authors. We tested the dye EvaGreen, a bis-intercalating dimeric acridine orange dye that is commonly used to detect dsDNA, but were unable to detect any fluorescence turn on from the microscopy experiments. We tested the performance of the dye in viral lysates and found that, when the lysate is digested with proteinase K, a much larger turn on is observed (Figure S7). This result suggests that EvaGreen cannot bind sufficiently to viral RNA complexed with proteins. We next tested a thioflavin T-derived dye ThT-NE which was previously described to bind to secondary structures of viral RNA inside cells.[23] However, no fluorescence turn on was observed with the microscopy-based viral fusion assay. Finally, we tested a recently developed

https://doi.org/10.1021/acs.analchem.4c01142
Anal. Chem. 2024, 96, 13033−13041

fluorogenic indolizine dye which was described to emit red fluorescence upon binding to cellular RNA;[24] however, we found that no fluorescence turn on was observed when we carried out a viral fusion assay (Figure S8A). We were unable to observe any appreciable fluorescence enhancement above the background in viral lysates as well even after proteinase K treatment (Figure S8B). In the subsequent experiments described in this paper, we used QuantiFluor as the sole content transfer dye. Unfortunately, the structure and concentration of QuantiFluor are not provided by the supplier, so we made a crude analysis to approximately determine the concentration of the working stock solution (Supporting Information and Methods, "Characterization of QuantiFluor" Figure S5).

Characterization of Fusion of Influenza Virus with Vesicles Encapsulating QuantiFluor. First, we sought to measure the kinetics of content transfer over a population of viruses bound to surface-tethered unilamellar vesicles (100 or 200 nm ULVs) encapsulating QuantiFluor. When the pH was dropped to 5.1, bright spots corresponding to fusion events were detected, which were followed by continuous imaging, and intensity traces were extracted from those videos (Figure 2A, SI Video 1, Figure S9). The time point (wait time) where we observed a sudden spike in intensity corresponded to the onset of the fusion event. Those wait times were then combined into the CDFs. From the CDFs, we observed that the content transfer kinetics of viruses with 100 nm was slightly faster than with 200 nm vesicles (Figure 2C). For comparison, we also carried out lipid mixing experiments between viruses labeled with self-quenching concentrations of Texas Red-DHPE and unlabeled 100 or 200 nm vesicles. In the event of fusion (or hemifusion), Texas Red-DHPE underwent dilution and a sudden spike in fluorescence was observed in the intensity traces (Figure 2B). We calculated the waiting time between the pH drop and appearance of a fluorescent spot and constructed CDFs to measure kinetics of lipid mixing (Figure 2C). In good agreement with previous results,[16,17] we found that lipid mixing took place at a more rapid rate as compared to that of content transfer.

Next, we estimated what fraction of virus particles undergoing lipid mixing also underwent content transfer. In this experiment, the influenza virus particles were labeled with a self-quenching concentration of Texas Red-DHPE, and fusion was carried out with QuantiFluor-containing vesicles. We identified the spots which underwent an increase in fluorescence in the Texas Red channel and also colocalized with a corresponding spot in the QuantiFluor channel (Figure S10). We roughly estimated that ∼40% (40 out of 99) of all vesicles undergoing lipid mixing underwent content transfer. It is notable here, however, that some vesicles may have too few or no trapped dye molecules, so that when content transfer took place to those vesicles, no signal would have been detectable. So, it is possible that the actual fraction of the virus-vesicle pairs undergoing content transfer may be somewhat underestimated.

Measuring the Distribution of vRNP Content upon Viral Fusion with Target Vesicles. During membrane fusion, efficient release of viral contents is decided by factors such as the sizes of the fusion pores.[25,26] The vRNPs of influenza are large structures measuring tens of nanometers (Figure S11), so it is not obvious that they will pass through the fusion pore even though small dye molecules may. The diameter of the fusion pore has been measured using cryogenic electron tomography (cryo-ET) and is estimated to be ∼15 nm at initial stages of fusion.[11,20,27] Therefore, for the transfer of vRNPs to the target

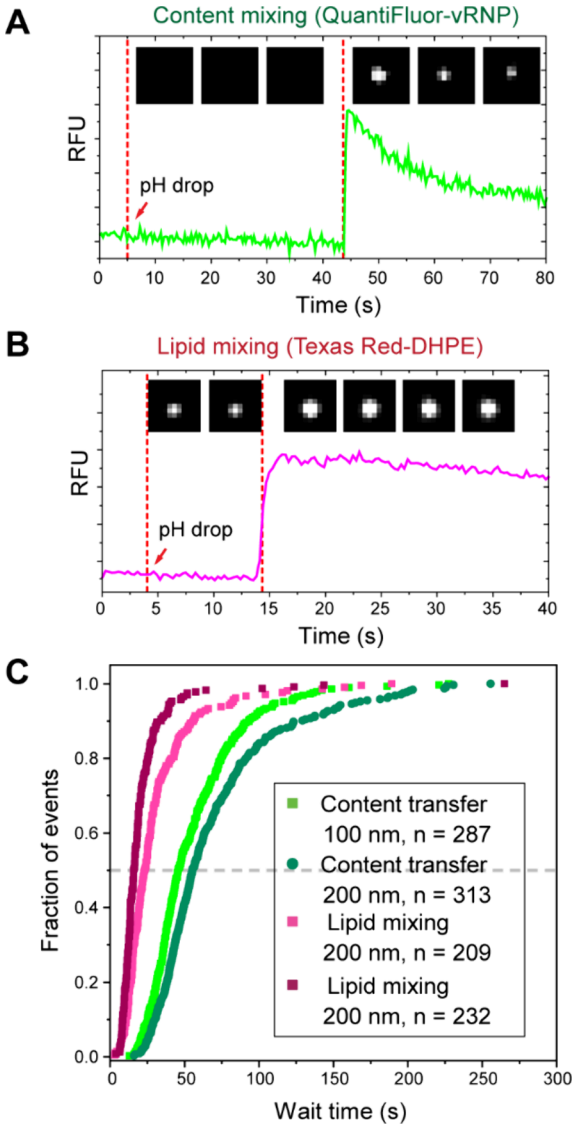

Figure 2. Fusion of the virus with target vesicles. (A) Fluorescence intensity profile corresponding to QuantiFluor fluorescence turn on during a typical content transfer event. (B) Fluorescence intensity profile corresponding to dequenching of Texas Red-DHPE fluorescence during a typical lipid mixing event. In A and B, micrographs corresponding to a single event are shown in the inset. (C) Cumulative distribution functions corresponding to content transfer and lipid mixing events for viral fusion with 100 and 200 nm vesicles.

vesicle, the fusion pore must expand to several tens of nanometers. Also, the vRNPs must dissociate fully from the M1 layer to freely distribute within the fused volume. Previous cryo-ET studies indeed revealed that two kinds of fused volumes may be obtained: (1) the virus and vesicle fused into a larger compartment, and the viral contents were evenly distributed; (2) the virus and vesicle compartments were connected through a narrow stalk-like pore, but the vRNPs were not transferred from the virus side.

We hypothesized that superlocalization microscopy techniques can be used to distinguish between the above two fusion scenarios since such techniques are widely used to pinpoint the centroid of a fluorescent particle with a lateral resolution of only a few tens of nanometers or less.[28,29] Although both the viruses[20] and vesicles (Figure S2B) have variable morphologies and sizes, given that the dimensions of the fused volume (150−250 nm) is

https://doi.org/10.1021/acs.analchem.4c01142
Anal. Chem. 2024, 96, 13033−13041

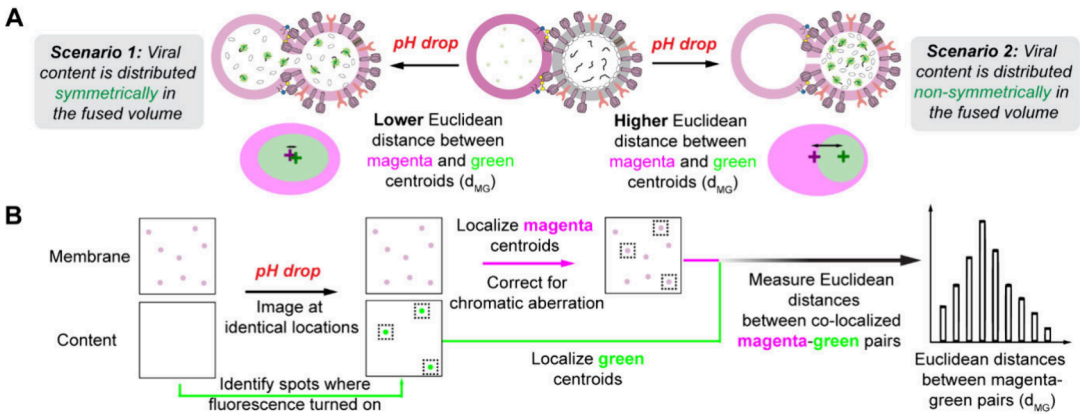

Figure 3. Schematic representation of an assay to measure the distribution of viral contents within the virus-vesicle fused volume. (A) When the vRNPs are symmetrically distributed within the fused volume, the centroids of the membrane (*magenta*) and content (*green*) signals overlap. If the viral contents are nonsymmetrically distributed within the fused volume, the centroids of the membrane (*magenta*) and content (*green*) signals are spaced farther apart. (B) Measurement of Euclidean distances between centroids of membrane (*magenta*) and content (*green*) signals (d_{MG}) using superlocalization and chromatic aberration correction procedures.

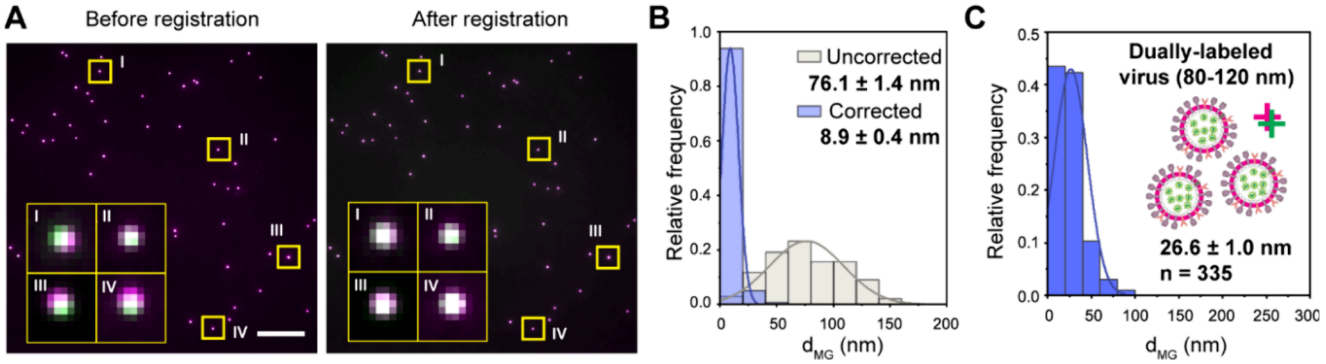

Figure 4. Superlocalization of objects in two channels. (A) Composite of two-channel images (488 nm channel in *green* and 561 nm channel in *magenta*) of multiply labeled 100 nm TetraSpeck beads before (*left*) and after (*right*) registration. Images of individual beads from different parts of the field-of-view (FOV) are shown in the inset. Scale bar: 20 μm. (B) Distribution of Euclidean distances between centroids of TetraSpeck beads in two channels (d_{MG}) in images "uncorrected" and "corrected" for chromatic aberration. (C) Distribution of d_{MG}'s for dually labeled virus particles. Data was binned into 20 nm intervals for all distributions. All error values denote standard error.

approximately at or below the diffraction limit (~200 nm), we assumed that the precise geometry of the latter will not have any significant effect on the superlocalization procedure. In the case of a large fusion pore, the dye-bound fluorescent vRNPs (content) will be evenly distributed within the fused volume, and the centroids of the signals from the membrane dye and the content dye should more or less overlap, therefore leading to a small Euclidean distance between them (*Scenario 1*, Figure 3A). In the case of formation of transient or small pores, the nucleic acid-binding dye (QuantiFluor), being a relatively small molecule (approximately 600 Da), will transfer to the virus side and bind there to the vRNPs remaining and turning on. The centroids of the signals from the membrane dye and the content dye should be farther apart, therefore leading to a larger Euclidean distance between them (*Scenario 2*, Figure 3A). Throughout the text and illustrations, the Euclidean distances between the centroids of the membrane (561 nm excitation, referred to as *magenta*) and content (488 nm excitation, referred to as *green*) channels are abbreviated as d_{MG}.

A schematic diagram outlining the procedure for measurement of d_{MG} values is illustrated in Figure 3B. Briefly, images are taken in *magenta* and *green* channels at various locations in the flow cell before fusion. The pH was then dropped to induce fusion, and after 30 min, images were obtained in 2 channels at identical positions to identify the locations of the turned-on green spots (QuantiFluor-RNA). We needed to precisely locate the centroids of the membrane and content signals to reliably measure the distances between them (Figure 3B). However, we had to address an important issue prior to carrying out distance measurements. While acquiring multichannel fluorescence images, the images acquired in different color channels are misaligned due to chromatic aberration.[30] Even though advanced objective lenses correct this aberration for most practical purposes, it can still limit superlocalization of diffraction-limited point sources.[31] Additionally, chromatic aberration is not uniform across the field-of-view (FOV).[31] The spectral channels need to be registered to reliably interpret the extent of colocalization between signals in two channels as outlined in Figure 3B. Channel registration was accomplished by imaging multiply labeled 100 nm TetraSpeck beads in *magenta* (561 nm excitation) and *green* (488 nm excitation) emission channels, with the latter being the reference channel. The centroids of the point spread functions of the spots were superlocalized using the FIJI plugin ThunderSTORM by 2D Gaussian fitting.[22] The chromatic calibration table containing the displacement vectors across the FOV were calculated using the FIJI plugin Detection of Molecules (DoM). which uses continuous smooth B-spline grid registration.[32] The coordinates

https://doi.org/10.1021/acs.analchem.4c01142
Anal. Chem. 2024, 96, 13033−13041

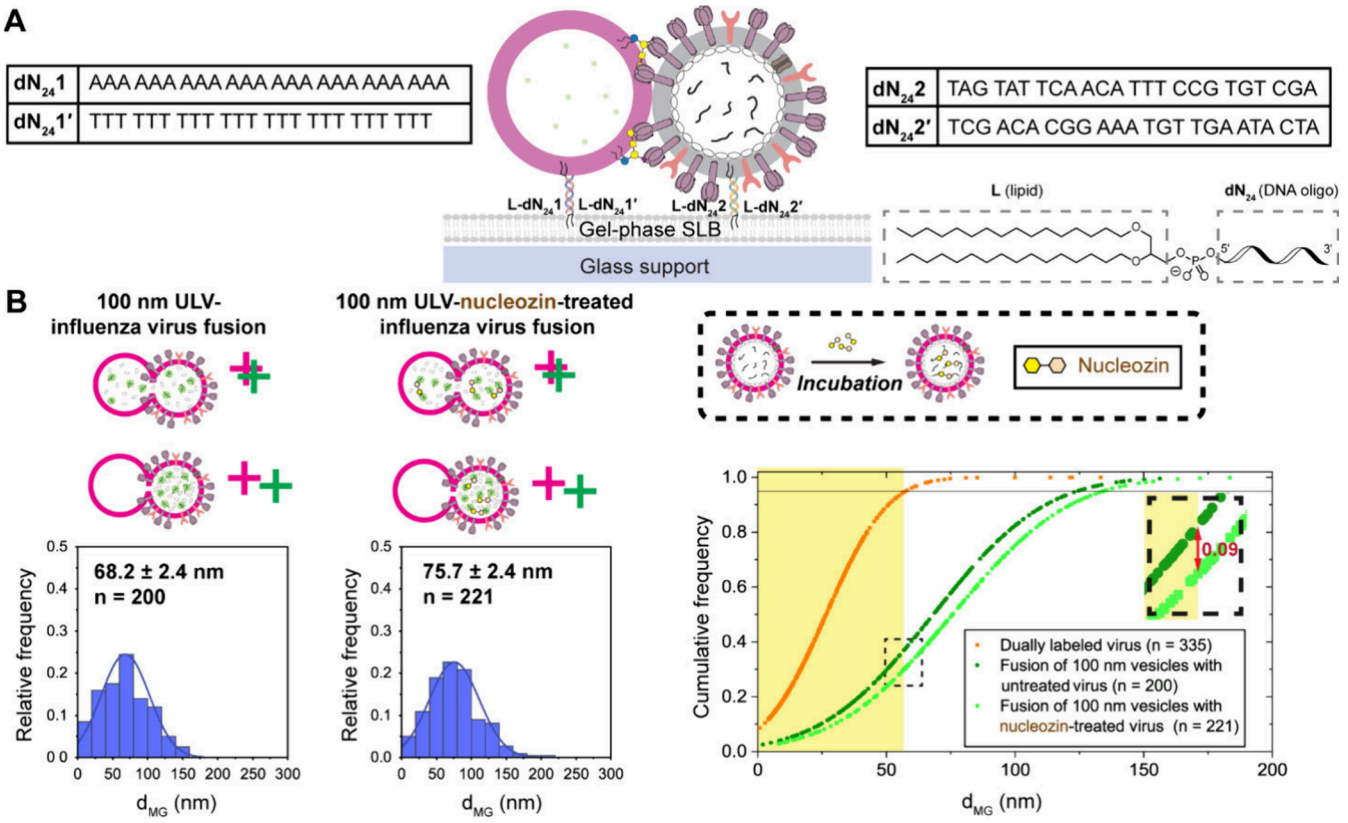

Figure 5. Fusion between virus particles and vesicles in a side-by-side configuration. (A) Vesicles (Texas Red-DHPE-labeled, encapsulating QuantiFluor and displaying GD1a) and influenza virus particles are sequentially tethered to a gel-phase (DPPC) supported lipid bilayer (SLB) via DNA-lipid conjugates (**L-dN$_{24}$**'s, 5′ → 3′ sequences in table) in a sidewise fashion. (B) Distribution of d_{MG}'s for fused volume between 100 nm vesicles and influenza viruses (untreated or treated with nucleozin). The size of the nucleozin molecule is exaggerated in the schematic diagram to highlight its effect on aggregation of vRNPs. The *magenta* and *green* colored "+" signs adjoining the schematics are used to denote whether the centroids in corresponding channels are expected to overlap or not. All error values denote standard error. Cumulative distribution function plots of d_{MG}'s for dually labeled influenza virus particles; fused volumes between 100 nm vesicles and untreated influenza virus; and fused volumes between 100 nm vesicles and influenza virus pretreated with nucleozin. The shaded region corresponds to distances less than 58 nm which is the value below which 95% of all the d_{MG}'s measured for dually labeled viruses belong.

of the spots in the *magenta* channel were corrected by vector transformation using the chromatic calibration table (Figure 4A). A distortion map generated with DoM illustrates the variability of the chromatic shift across the FOV (Figure S12). Following this, d_{MG} values were calculated using ThunderSTORM. It was found that, in uncorrected calibration set images, d_{MG} values of approximately 0−140 nm were measured with a mean of 76.1 ± 1.4 nm (Figure 4B). In the corrected images, d_{MG} ranged only over 0−50 nm with a mean of 8.9 ± 0.4 nm (Figure 4B).

We tested the performance of our distance measurement method taking a few cases where the centroids of *magenta* and *green* signals should colocalize. First, we analyzed images of TetraSpeck beads separate from the images used for calibration. In the corrected images, we measured a narrow distribution of d_{MG} with a mean of 11.0 ± 0.2 nm. Next, we calculated the d_{MG} for 50, 100, and 200 nm vesicles having membrane stained with Texas Red-DHPE and encapsulating Alexa Fluor 488. We obtained values of 29.2 ± 0.5, 25.7 ± 0.8, and 20.7 ± 0.7 nm, respectively (Figure S13). To test the performance with alternate green-emitting fluorescent dyes, we measured d_{MG} for Texas Red-DHPE labeled 100 nm vesicles encapsulating carboxyfluorescein and pyranine and obtained values of 28.2 ± 0.6 nm and 28.9 ± 0.4 nm, respectively (Figure S13).

Finally, we sought to test a dually labeled system that best represented the fluorescence signal level expected in an actual fusion experiment. We found that the RNA of intact influenza virus particles can be fluorescently labeled by incubating a virus suspension with a buffer containing QuantiFluor, similar to previously described methods for labeling of viral genomes.[33,34] We prepared virus particles with the lipid membrane labeled with Texas Red-DHPE and the RNA labeled with QuantiFluor. Dually labeled virus particles adsorbed to plasma-cleaned glass surface were imaged, and a mean d_{MG} value of 26.6 ± 1.0 nm was measured (Figure 4C). We combined all d_{MG} distributions from objects with fully colocalizing *magenta* and *green* signals into cumulative distribution functions and determined the d_{MG} value below which 95% of the distances lie (Figure S14). In the case of dually labeled virus particles, 95% of d_{MG} values were below 58 nm, which may be chosen as the limiting value below which two signals may be interpreted as fully overlapping. Therefore, we arbitrarily chose 58 nm as the cutoff value to distinguish between symmetric (<58 nm) and nonsymmetric (>58 nm) content distribution obtained in the viral fusion experiments as will be described in the next sections.

To measure the viral content distribution within the fused volume as illustrated in Figure 3A, ideally, the viral fusion experiment needs to be carried out in a configuration where the virus and vesicle are placed side-by-side. Initially, we attempted

https://doi.org/10.1021/acs.analchem.4c01142
Anal. Chem. 2024, 96, 13033−13041

to obtain this information by carrying out fusion between virus particles with vesicles tethered to a PLL−PEG coated surface as illustrated in Figure 1B. We obtain a distribution of d_{MG} values ranging roughly between 0 and 150 nm with a mean of 59.9 ± 2.2 nm (Figure S15A), a value significantly higher than the corresponding d_{MG} values (<30 nm) obtained for objects where two signals are perfectly overlapping as shown in Figure 4C and Figure S13. The data clearly indicates that many fusion events were characterized by a nonsymmetric content distribution which is expected to yield larger d_{MG} values as compared to symmetric content distribution. However, we must also consider that, in this fusion configuration, from simple geometric arguments, there will be certain limiting conditions where a symmetric and nonsymmetric fused volume will be indistinguishable. For example, a virus bound near the polar regions of a vesicle (as schematically shown in Figure 1B) will lead to nearly identical d_{MG} values for both symmetric and nonsymmetric modes of fusions (Figure S15B). In such situations, the d_{MG} values will be underestimated for nonsymmetric fused volumes.

Inspired by a previously described strategy for vesicle tethering,[35] we designed an experimental configuration where it is possible to increase the likelihood for viruses to bind close to the equatorial regions of the target vesicles and achieve fusion in a side-by-side configuration. We prepared a supported lipid bilayer (SLB) using the gel-phase (at room temperature) forming lipid dipalmitoylphosphatidylcholine (DPPC) and small fractions of two sets of orthogonal DNA-lipid conjugates (**L-dN$_{24}$1** and **L-dN$_{24}$2**, Figure 5A)[35,36] that can serve as binding sites for objects (vesicles and viruses) bearing DNA-lipid conjugates with complementary sequences (i.e., **L-dN$_{24}$1′** and **L-dN$_{24}$2′**, respectively). We chose a mole fraction of the DNA-lipid conjugates with respect to DPPC such that there are approximately 4 DNA-lipid conjugates of each type on average within a 100 × 100 nm region of the SLB. We assumed that some virus particles incorporating a DNA-lipid conjugate will initially dock at pH 7.4 on to vesicles via GD1a receptors, following which they will also tether strongly to the SLB by hybridizing with a nearby complementary DNA sequence. In this way, a virus-vesicle pair can be positioned next to each other on the SLB and, because of the gel nature of the SLB, they will not be free to diffuse, essential for the superlocalization measurements described in the following. Also, the gel-phase membranes are expected to be mechanically stiffer than fluid phase membranes, and therefore, the virus particles are not expected to fuse to the SLB itself.[37] We first tethered target vesicles displaying GD1a to the SLB via the DNA-lipid conjugate **L-dN$_{24}$1′** (Figure 5A) and washed away unbound vesicles (Figure S16A). In control conditions where no DNA-lipid conjugate was added to the SLB or the target vesicles or both, no or minimal tethering of vesicles to the SLBs was detected. Next, we added the virus particles preincubated with DNA-lipid conjugate **L-dN$_{24}$2′** and allowed them to simultaneously attach to GD1a receptors on the vesicle surface and to the DNA strand on the SLB surface. We noted that attachment of a virus particle next to a vesicle is an inherently low probability event. Only 10 virus particles (internally labeled with QuantiFluor) per 1000 target vesicles were observed to tether to the SLB via DNA-lipid conjugates next to a vesicle when the vesicles lacked GD1a. However, when GD1a was present on the vesicles, the probability of association increased ∼4 times (43 per 1000) (Figure S17).

We measured the d_{MG} within a fused volume between 100 nm vesicles and viruses and obtained a significantly broader distribution of d_{MG}'s ranging between 0 and 150 nm and a mean of 68.2 ± 2.4 nm (Figure 5B). This value is significantly larger than that obtained for the fusion of virus particles with 100 nm vesicles tethered to a PLL−PEG surface (Figure S15A), which suggests that the tethering strategy in Figure 5A indeed increases the probability of side-by-side fusion. To test the consistency of our methodology, we asked whether the range of measured d_{MG} values increases if the size of the fused volume is increased. We carried out fusion between 200 nm vesicles and viruses, and indeed d_{MG} values were spread over larger range (0−250 nm) with a significantly higher mean of 82.4 ± 2.8 nm (Figure S18) as compared to the case with 100 nm vesicles.

Next, we sought to test the effect of a drug that is likely to influence the passage of vRNPs through the fusion pore. Nucleozin is a small molecule drug which is known to cause aggregation of vRNPs *in cellulo* or *in vitro* via bridging NPs together.[7,38] Therefore, we hypothesized that influenza virus particles treated with nucleozin will contain aggregated vRNPs which will be less likely to pass through the fusion pores and therefore lead to higher d_{MG} values. Influenza virus particles were incubated with nucleozin and then allowed to cotether with vesicles to the SLB surface as described above. Interestingly, we measured a broader distribution of d_{MG} values and a higher mean value of 75.7 ± 2.4 nm (Figure 5B) as compared to the case of fusion of an identical preparation of vesicles with an identical batch of untreated viruses (68.2 ± 2.4 nm) (representative images of fusion experiments provided in Figure S19). The d_{MG}'s from viral fusion experiments along with those from dually labeled influenza virus (Figure 4C) were plotted into a cumulative distribution function (Figure 5B). As discussed earlier, since 95% of the d_{MG}'s for the dually labeled influenza virus fall below 58 nm, we chose this number as a cutoff value for distinguishing between symmetric (<58 nm) and nonsymmetric (>58 nm) modes of fusion. In the case of untreated sample, 39% of all d_{MG}'s fell below 58 nm while in the case of the nucleozin-treated sample, 30% of all d_{MG}'s fell below 58 nm (Figure 5B). The data support our initial hypothesis that nucleozin causes aggregation of vRNPs and the aggregated vRNPs transfer through the fusion pore less efficiently. Given that this analysis is subject to key assumptions such as choice of cutoff value for d_{MG}, we suggest that the results should be interpreted in a semiquantitative and relative sense rather than an absolute measure. Also, to derive meaningful conclusions, a comparison between like systems should be made. Although nucleozin has been described to exert its anti-influenza action by causing nucleoprotein aggregation in the cytoplasm and thereby prevent its nuclear import,[39] its effect on the endosomal escape has not been reported so far. Therefore, based on our prediction, it will be interesting to discover whether nucleozin and other nucleoprotein-binding drugs[40−42] can be found to exert inhibitory effects on viral content release in cell-based studies as well.

CONCLUSION

In summary, we developed a method based on the pseudoinfection model to visualize the transfer and distribution of viral macromolecular contents to target vesicles. Until now, this model has been utilized to characterize the earliest stages of viral infection, such as binding of virus particles to membrane-bound receptors and mixing of viral and vesicular lipid compartments and contents. From previous content mixing assays based on the dequenching of water-soluble dyes, it was not possible to infer whether the viral contents themselves completely mixed within the fused volume. Also, in a previous

https://doi.org/10.1021/acs.analchem.4c01142
Anal. Chem. 2024, 96, 13033−13041

genome exposure assay,[17] the issue of distribution of viral contents within the fused volume was not addressed. Here, we show that the utility of the pseudoinfection model can be expanded to probe the distribution of viral contents within the fused volume. Whereas in the past the question of viral content distribution has been addressed using structural techniques such as cryo-ET, we showed that relatively simpler fluorescence microscopy-based measurements can be used to derive such spatial information.

In our method, detection of a content transfer event implies that a virus particle has functional fusion proteins, contains nucleic acid, and forms a fusion pore, all of which are necessary conditions of infectivity. Due to the fluorogenic nature of QuantiFluor, detection of fusion events is essentially background-free, so counting of such events (i.e., new fluorescent spots) is straightforward, and minimally prone to artifacts and spurious events. Also, our method is suitable for studying the fusion behavior of any enveloped virus given that the viral receptor−ligand pair is known. We foresee that our method of probing viral content transfer to target vesicles using a fluorogenic dye will find many applications in virology and related disciplines. For example, viral infectivity is typically measured using cell culture-based methods which are expensive and time-consuming.[43] Therefore, alternate methods for quantification of viral infectivity that are rapid and do not require cell cultures are highly desirable. Cell-free measurement of viral infectivity may allow assessment of the effects of antiviral therapeutics like neutralizing antibodies[44] or small molecules[45] which block cellular entry or inhibitors of fusion pore formation like IFITM3[46] in a straightforward manner. Indeed, our preliminary experiments with virus particles (0.2 mg/mL protein) incubated with broadly neutralizing antibodies CR9114 (4 μM) and MEDI8852 (4 μM) showed 91% and 88% less fusion events, respectively, as compared to the case where the viruses were not treated with antibodies (Figure S20). Cell-free methods will also be beneficial for measuring infectivities of BSL-3 agents like highly pathogenic avian influenza (HPAI) A strain H5N1 and SARS-CoV-2 rapidly while generating minimal biohazardous waste, which will facilitate pandemic preparedness research. Therefore, as a next step, it will be interesting to investigate whether counting the number of full fusion events can be directly correlated to viral infectivity obtained from cell-based assays, and such efforts are currently underway.

Our incorporation of superlocalization microscopy principles into the pseudoinfection model will expand its utility to address many general problems in membrane biophysics dealing with the efficiency of transfer of vesicular contents. For example, our method will be useful to interrogate the mechanistic details of agents which are thought to restrict expansion of fusion pores induced by viral fusion proteins.[12,47,48] It will also be possible to interrogate whether viral proteins alone are sufficient for fusion pore stabilization and expansion or whether host cellular factors have a role.[49] An improvement in photophysical properties of the RNA-binding dye will allow sequential imaging, which will allow for studying the evolution of the content distribution pattern as a function of time. Finally, we foresee that our method of content distribution assay based on superlocalization microscopy can be further adopted for estimating the efficiency of endosomal escape of cellular nanocarriers like lipid nanoparticles (LNPs) or vectors based on enveloped viruses which is still largely an empirical subject.[50−52] A reliable and straightforward measure of the content distribution between such nanocarriers and target vesicles (mimicking the endosome membrane) will be expected to better reflect its endosomal escape behavior and thus facilitate the rational design of the former.

■ ASSOCIATED CONTENT

Supporting Information

The Supporting Information is available free of charge at https://pubs.acs.org/doi/10.1021/acs.analchem.4c01142.

Supporting materials and methods, summary of the fluorogenic nucleic acid-binding dyes, dyes with known chemical structures used in this work, preparation and characterization of unilamellar vesicles, schematic of experimental setup, screening of nucleic-acid binding dyes, characterization of QuantiFluor, semi-qualitative comparison of the photostability, tests of EvaGreen and an indolizine dye as content transfer assay dyes, fluorescence intensity traces, images of 100 nm vesicles undergoing lipid mixing and content transfer, TEM images, distortion map of chromatic aberration, distribution of d_{MG}'s, distributions of Euclidean distances, gel-phase supported lipid bilayers, side-by-side tethering of viruses and vesicles, fluorescence micrographs, and cell-free assessment of inhibitory effects (PDF)

SI Video 1 (AVI)

SI Video 2 (AVI)

■ AUTHOR INFORMATION

Corresponding Author

Steven G. Boxer − *Department of Chemistry, Stanford University, Stanford, California 94305, United States;* orcid.org/0000-0001-9167-4286; Email: sboxer@stanford.edu

Authors

Ahanjit Bhattacharya − *Department of Chemistry and Stanford Center for Innovation in Global Health, Stanford University, Stanford, California 94305, United States;* orcid.org/0000-0001-6810-9537

Nahal Bagheri − *Department of Electrical Engineering, Stanford University, Stanford, California 94305, United States*

Complete contact information is available at: https://pubs.acs.org/10.1021/acs.analchem.4c01142

Author Contributions

A.B. and S.G.B conceived the project. A.B. designed and performed the experiments and analyzed the data. N.B. wrote the MATLAB code, and analyzed the data for content transfer kinetic analysis. A.B. wrote the manuscript under the guidance of S.G.B.

Notes

The authors declare no competing financial interest.

■ ACKNOWLEDGMENTS

This work was supported in part by NIH Grant GM118044 (to S.G.B.). We thank Dr. Frank R. Moss III (SLAC National Accelerator Laboratory) for cryo-TEM imaging of vesicles, the Moerner lab for 0.1 μm TetraSpeck microsphere beads, and Professor Chao Zhang (University of Southern California) for the indolizine dye. We thank Drs. Katherine N. Liu, Srijit Mukherjee, Robert J. Rawle (Williamson College), and Anish Raj Roy (W.E. Moerner Lab) for helpful discussions.

REFERENCES

(1) White, J. M.; Ward, A. E.; Odongo, L.; Tamm, L. K. *Annu. Rev. Virol.* **2023**, *10* (1), 139−161.
(2) Benhaim, M. A.; Lee, K. K. *Viruses* **2020**, *12* (4), 413.
(3) Fontana, J.; Steven, A. C. *Arch. Biochem. Biophys.* **2015**, *581*, 86−97.
(4) Haldar, S. *J. Membr. Biol.* **2022**, *255* (6), 747−755.
(5) Banerjee, S.; Maurya, S.; Roy, R. *J. Biosci.* **2018**, *43* (3), 519−540.
(6) Hutchinson, E. C.; Charles, P. D.; Hester, S. S.; Thomas, B.; Trudgian, D.; Martínez-Alonso, M.; Fodor, E. *Nat. Commun.* **2014**, *5* (May), 4816.
(7) Coloma, R.; Arranz, R.; de la Rosa-Trevín, J. M.; Sorzano, C. O. S.; Munier, S.; Carlero, D.; Naffakh, N.; Ortín, J.; Martín-Benito, J. *Nat. Microbiol.* **2020**, *5* (5), 727−734.
(8) Noda, T.; Sagara, H.; Yen, A.; Takada, A.; Kida, H.; Cheng, R. H.; Kawaoka, Y. *Nature* **2006**, *439* (7075), 490−492.
(9) Coloma, R.; Valpuesta, J. M.; Arranz, R.; Carrascosa, J. L.; Ortín, J.; Martín-Benito, J. *PLoS Pathog.* **2009**, *5* (6), No. e1000491.
(10) Selzer, L.; Su, Z.; Pintilie, G. D.; Chiu, W.; Kirkegaard, K. *PLoS Biol.* **2020**, *18* (9), No. e3000827.
(11) Lee, K. K. *EMBO J.* **2010**, *29* (7), 1299−1311.
(12) Staring, J.; Raaben, M.; Brummelkamp, T. R. *J. Cell Sci.* **2018**, *131* (15), jcs216259.
(13) Park, C.; Kim, E.; Park, G.; Kim, B. C.; Vellampatti, S.; Lim, J.-W.; Lee, S.; Chung, S.; Jun, S.-H.; Lee, S.; Ali, S.; Yeom, M.; Song, D.; Haam, S. *Adv. Funct. Mater.* **2023**, *33*, 2214603.
(14) Chernomordik, L. V.; Kozlov, M. M. *Nat. Struct. Mol. Biol.* **2008**, *15* (7), 675−683.
(15) Floyd, D. L.; Ragains, J. R.; Skehel, J. J.; Harrison, S. C.; Van Oijen, A. M. *Proc. Natl. Acad. Sci. U. S. A.* **2008**, *105* (40), 15382−15387.
(16) Liu, K. N.; Boxer, S. G. *Biophys. J.* **2021**, *120* (21), 4832−4841.
(17) Villamil Giraldo, A. M.; Mannsverk, S.; Kasson, P. M. *Biophys. J.* **2022**, *121* (23), 4467−4475.
(18) Hughes, L. D.; Rawle, R. J.; Boxer, S. G. *PLoS One* **2014**, *9* (2), No. e87649.
(19) Chou, Y.-y.; Vafabakhsh, R.; Doganay, S.; Gao, Q.; Ha, T.; Palese, P. *Proc. Natl. Acad. Sci. U. S. A.* **2012**, *109* (23), 9101−9106.
(20) Gui, L.; Ebner, J. L.; Mileant, A.; Williams, J. A.; Lee, K. K. *J. Virol.* **2016**, *90* (15), 6948−6962.
(21) Chlanda, P.; Mekhedov, E.; Waters, H.; Schwartz, C. L.; Fischer, E. R.; Ryham, R. J.; Cohen, F. S.; Blank, P. S.; Zimmerberg, J. *Nat. Microbiol.* **2016**, *1* (6), 16050.
(22) Ovesný, M.; Křížek, P.; Borkovec, J.; Švindrych, Z.; Hagen, G. M. *Bioinformatics* **2014**, *30* (16), 2389−2390.
(23) Luo, X.; Xue, B.; Feng, G.; Zhang, J.; Lin, B.; Zeng, P.; Li, H.; Yi, H.; Zhang, X. L.; Zhu, H.; Nie, Z. *J. Am. Chem. Soc.* **2019**, *141* (13), 5182−5191.
(24) Kim, M. J.; Li, Y.; Junge, J. A.; Kim, N. K.; Fraser, S. E.; Zhang, C. *ACS Chem. Biol.* **2023**, *18*, 1523−1533.
(25) Melikyan, G. B.; Niles, W. D.; Ratinov, V. A.; Karhanek, M.; Zimmerberg, J.; Cohen, F. S. *J. Gen. Physiol.* **1995**, *106* (5), 803−819.
(26) Markosyan, R. M.; Miao, C.; Zheng, Y. M.; Melikyan, G. B.; Liu, S. L.; Cohen, F. S. *PLoS Pathog.* **2016**, *12* (1), No. e1005373.
(27) Calder, L. J.; Rosenthal, P. B. *Nat. Struct. Mol. Biol.* **2016**, *23* (9), 853−858.
(28) Möckl, L.; Moerner, W. E. *J. Am. Chem. Soc.* **2020**, *142* (42), 17828−17844.
(29) Wang, J.; Han, M.; Roy, A. R.; Wang, H.; Möckl, L.; Zeng, L.; Moerner, W. E.; Qi, L. S. *Cell Reports Methods* **2022**, *2* (2), 100170.
(30) Erdelyi, M.; Rees, E.; Metcalf, D.; Schierle, G. S. K.; Dudas, L.; Sinko, J.; Knight, A. E.; Kaminski, C. F. *Opt. Express* **2013**, *21* (9), 10978.
(31) Eliscovich, C.; Shenoy, S. M.; Singer, R. H. *Proc. Natl. Acad. Sci. U. S. A.* **2017**, *114* (10), E1875−E1884.
(32) *Detection of Molecules (DoM) plugin v.1.2.4 for ImageJ*; https://github.com/UU-cellbiology/DoM_Utrecht.
(33) Liu, S. L.; Tian, Z. Q.; Zhang, Z. L.; Wu, Q. M.; Zhao, H. S.; Ren, B.; Pang, D. W. *Biomaterials* **2012**, *33* (31), 7828−7833.
(34) Zamora, J. L. R.; Aguilar, H. C. *Methods* **2018**, *2018* (134−135), 87−97.
(35) Van Lengerich, B.; Rawle, R. J.; Boxer, S. G. *Langmuir* **2010**, *26* (11), 8666−8672.
(36) Chan, Y.-H. M.; van Lengerich, B.; Boxer, S. G. *Biointerphases* **2008**, *3* (2), FA17−FA21.
(37) Norling, K.; Sjöberg, M.; Bally, M.; Zhdanov, V. P.; Parveen, N.; Höök, F. *Langmuir* **2022**, *38* (8), 2550−2560.
(38) Kao, R. Y.; et al. *Nat. Biotechnol.* **2010**, *28* (6), 600−605.
(39) Amorim, M. J.; Kao, R. Y.; Digard, P. *J. Virol.* **2013**, *87* (8), 4694−4703.
(40) Gerritz, S. W.; et al. *Proc. Natl. Acad. Sci. U. S. A.* **2011**, *108* (37), 15366−15371.
(41) Yang, F.; Pang, B.; Lai, K. K.; Cheung, N. N.; Dai, J.; Zhang, W.; Zhang, J.; Chan, K.-H.; Chen, H.; Sze, K.-H.; Zhang, H.; Hao, Q.; Yang, D.; Yuen, K.-Y.; Kao, R. Y. *J. Virol.* **2021**, *95* (9), No. e01432.
(42) Correa-Padilla, E.; Hernández-Cano, A.; Cuevas, G.; Acevedo-Betancur, Y.; Esquivel-Guadarrama, F.; Martinez-Mayorga, K. *PLoS One* **2023**, *18* (2), No. e0277073.
(43) McCracken, R.; Al-Nazal, N.; Whitmer, T.; Yi, S.; Wagner, J. M.; Hebert, C. G.; Lowry, M. J.; Hayes, P. R.; Schneider, J. W.; Przybycien, T. M.; Mukherjee, M. *Vaccines* **2022**, *10* (10), 1589.
(44) Paules, C. I.; Lakdawala, S.; McAuliffe, J. M.; Paskel, M.; Vogel, L.; Kallewaard, N. L.; Zhu, Q.; Subbarao, K. *J. Infect. Dis.* **2017**, *216* (3), 356−365.
(45) Yao, Y.; Kadam, R. U.; Lee, C. C. D.; Woehl, J. L.; Wu, N. C.; Zhu, X.; Kitamura, S.; Wilson, I. A.; Wolan, D. W. *Proc. Natl. Acad. Sci. U. S. A.* **2020**, *117* (31), 18431−18438.
(46) Bailey, C. C.; Zhong, G.; Huang, I. C.; Farzan, M. *Annu. Rev. Virol.* **2014**, *1* (1), 261−283.
(47) Ciechonska, M.; Duncan, R. *J. Virol.* **2014**, *88* (11), 6528−6531.
(48) Rosa, A.; Chande, A.; Ziglio, S.; De Sanctis, V.; Bertorelli, R.; Goh, S. L.; McCauley, S. M.; Nowosielska, A.; Antonarakis, S. E.; Luban, J.; Santoni, F. A.; Pizzato, M. *Nature* **2015**, *526* (7572), 212−217.
(49) Melikyan, G. B. *Retrovirology* **2008**, *5*, 111.
(50) Dowdy, S. F. *Rna* **2023**, *29* (4), 396−401.
(51) Mehta, M. J.; Kim, H. J.; Lim, S. B.; Naito, M.; Miyata, K. *Macromol. Biosci.* **2024**, *24*, 2300366.
(52) Winter, S. L.; Chlanda, P. *Subcell. Biochem.* **2023**, *106*, 113−152.

https://doi.org/10.1021/acs.analchem.4c01142
Anal. Chem. 2024, 96, 13033−13041

Supporting Information

A fluorogenic pseudo-infection assay to probe transfer and distribution of influenza viral contents to target vesicles

Ahanjit Bhattacharya,[1, 2] Nahal Bagheri,[3] Steven G. Boxer[1, *]

[1]Department of Chemistry, Stanford University, Stanford, CA-94305

[2]Stanford Center for Innovation in Global Health, Stanford University, Stanford CA-94305

[3]Department of Electrical Engineering, Stanford University, Stanford, CA-94305

*Correspondence to: sboxer@stanford.edu

This PDF file includes:

Supplementary Materials and Methods
Supplementary Figures. S1 to S20
Supplementary Video captions
Supplementary References

Other supporting materials for this manuscript include the following:

MATLAB code for analyzing content transfer data is available at https://github.com/boxerlab/Content-Transfer.

Supplementary Materials and Methods

Chemicals and general considerations. Palmitoyl oleoyl phosphatidylcholine (POPC), dioleoyl phosphatidylethanolamine (DOPE), dipalmitoyl phosphatidylcholine (DPPC), cholesterol, and 16:0 Biotinyl Cap PE were purchased from Avanti Polar Lipids (Alabaster, AL). Texas Red-1,2-dihexadecanoyl-*sn*-glycero-3-phosphoethanolamine (Texas Red-DHPE), Alexa Fluor 488 (succinimidyl ester), and NeutrAvidin were purchased from Thermo Fisher Scientific. Sepharose CL-4B, disialoganglioside GD1a (from bovine brain), and IGEPAL were purchased from Sigma-Aldrich. Chloroform, methanol, HEPES buffer, and buffer salts were obtained from Fisher Scientific and Sigma-Aldrich. Polydimethylsiloxane (PDMS) was obtained from Ellsworth Adhesives (Hayward, CA). Poly(L-lysine)-graft-poly(ethylene glycol) and poly(L-lysine)-graft-poly(ethylene glycol) biotin were purchased from SuSoS (Dübendorf, Switzerland). Nucleozin was purchased from Cayman Chemicals. Proteinase K was purchased from Thermo Fisher Scientific.

Preparation of buffers. The following buffers were used, and osmolality values were measured on an Advanced Instruments Micro-Osmometer 3320:

Vesicle buffer: 10 mM Na-phosphate, 90 mM Na-citrate, and 150 mM NaCl (pH 7.4). Osmolality: 545 mOsmol/kg.

Fusion buffer: 10 mM Na-phosphate, 90 mM Na-citrate, and 150 mM NaCl (pH 5.1). Osmolality: 510 mOsmol/kg.

Lysis buffer: 100 mM Tris (pH 7.5), 100 mM NaCl, 5 mM $MgCl_2$, 3 mM DTT, 1% (v/v) IGEPAL.

Microscopy. Fluorescence images were acquired with a Nikon Ti-U microscope using a 100X oil immersion apochromat TIRF objective (NA = 1.49) (Nikon Instruments, Melville, NY). A Spectra-X LED Light Engine (Lumencor, Beaverton, OR) was used for illumination, and an Andor iXon 897 EMCCD camera (Andor Technologies, Belfast, UK) with 16-bit image settings. Images were captured with Metamorph software version 7.7.11.0 (Molecular Devices, Sunnyvale, CA).

Vesicle preparation. A lipid mixture composed of POPC:DOPE:Cholesterol:GD1a:Biotin-DPPE:TR-DHPE by molar ratio of 37.4:20:40:2:0.5:0.1 dissolved in organic solvents (chloroform and methanol) was taken in a glass vial. The solvents were removed under a flow of argon gas, and the film was dried under house vacuum for at least 12 h. The hydration solution containing a nucleic acid-binding dye is added to the vial and the film is hydrated by vortexing. We targeted a bulk concentration of 10-100 µM for a given dye to ensure encapsulation of tens of molecules in a single vesicle. The dispersion is transferred to a 0.6 mL tube and then freeze-thawed 5 times. The dispersion was next extruded through 100 nm or 200 nm polycarbonate filters using a mini extruder device (Avanti Polar Lipids) at least 31 times. The vesicles were purified on a small size-exclusion column packed with Sepharose CL-4B gel (0.8-1 mL wet volume). Eluent was collected in small fractions (70-90 µL) in 0.2 mL tubes. The fractions containing vesicles were identified from Texas Red-DHPE fluorescence by checking the tubes under UV lamp. Vesicle suspensions were stored at 4 °C and typically used within 2 months even though we found that vesicles encapsulating QuantiFluor were stable for over 1 year when stored at 4 °C and can be used successfully for the content transfer experiments. We measured the size distribution and polydispersity of the vesicles using dynamic light scattering using a NanoBrook Omni particle size and zeta potential analyzer (Brookhaven Instruments). For typical vesicle preparations, we measured effective diameters (d_{eff}) of 124.8±2.9 nm (polydispersity = 0.061) and 160.0±3.4 nm (polydispersity = 0.274) for vesicles generated by extrusion through 100 nm and 200 nm membrane filters respectively (Figure S2A). For simplicity, we refer to the above two kinds of vesicles as 100 nm and 200 nm vesicles or unilamellar vesicles (ULVs). The 100

nm vesicles were imaged by cryo-TEM to check for unilamellarity (Figure S2B). Most vesicles were found to be unilamellar with some showing multi-compartment (vesicle-in-vesicle) architecture.

Influenza virus preparation. Influenza A virus (strain X-31, A/Aichi/68, H3N2) grown in the allantoic cavity of specific pathogen-free (SPF) eggs was purchased from Charles River Laboratories (Wilmington, MA). The main stock (HA titer: 32768/0.05 mL, EID_{50}: $10^{9.5}$/mL, protein content: 2 mg/mL) was stored as 20 µL aliquots at -80 °C until use. Influenza A Virus is a Biosafety Level 2 agent and was handled following an approved biosafety protocol developed at Stanford University. The commercially purchased virus suspension was directly diluted in *vesicle buffer* for use in content transfer experiments. DNA lipid conjugates were incorporated into the influenza virus membrane by incubating virus sample at 4 °C on ice overnight.

Viruses were lysed by incubating a suspension (15-20 µL of commercially available stock, protein concentration ~2 mg/mL) with 100 µL *lysis buffer* at 37 °C for 1 h. The insoluble debris was removed by centrifugation at 21,130 rcf for 30 min at 4 °C. The supernatant (~110 µL) was collected for studying the turn-on behavior of the nucleic acid binding dyes. In case of QuantiFluor, the final dye concentration added to the supernatant was approximately 10 µM and it was kept incubated at RT for 30 min. The supernatant was also used for TEM imaging of vRNPs (Figure S11). In the experiments where proteinase K digestion was performed, SDS-PAGE was carried out to confirm that the viral proteins were completely digested.

Note on dyes. See Figure S1 for structures of dyes where available. We communicated with the technical support division of Biotium and confirmed that Oxazole Gold is identical to SYBR Gold available from other suppliers. Biotium also informed us that the stock solution of Thiazole Green (SYBR Green I) has a concentration of ~10 mM. We preferred to prepare vesicles in the absence of any DMSO which may affect membrane properties, so we attempted to remove DMSO from each commercially available dye stock solution by lyophilization and re-dissolved the residue in Milli-Q water. We found that the SYTO family of dyes could not be re-dissolved in this manner and most of the dye remained stuck to the plastic tube walls. Overall, the SYTO (11-14, 16, 21, 24, 25) dyes were found to be completely unsuitable for content transfer experiments. Most of these dyes tended to form aggregates during vesicle preparation due to apparent hydrophobicity, and we were unable to detect any turn-on behavior in the microscopy experiments. Moreover, in the case of SYTO 12, when an aqueous solution of the dye was made, the yellow color faded within 30 min, suggesting that the compound may be unstable. Only EvaGreen was commercially available as an aqueous solution (25 µM) and it was concentrated to 0.5 mM. Indolizine dye (Table S1, Figure S9) was soluble in water and stored as a 1 mM stock solution. A few simple mathematical calculations were useful as a guide to choose the concentration of a dye in the hydration solution: (i) if the concentration of a molecule in bulk is 100 µM, there are ~30 molecules inside of a 100 nm vesicle (ii) if the concentration of a molecule in bulk is 10 µM, there are ~3 molecules inside of a 100 nm vesicle.

Characterization of QuantiFluor. QuantiFluor® (Promega) is a commercially available dye whose structure and concentration are currently proprietary. We carried out a few characterizations of the dye to roughly estimate the concentration. 500 µL of deep orange colored DMSO solution obtained from Promega was mixed with 5 mL of Milli-Q water, lyophilized, and the measured mass of the orange residue was approximately 0.30 mg. This residue was dissolved in 500 µL Milli-Q water, aliquoted into smaller volumes and stored at -20 °C. The aqueous solution is stable at room temperature for several weeks when kept in dark. The turn-on properties of the dye with RNA remained unchanged through the lyophilization/re-dissolving process. We found that the residue could be re-dissolved in Milli-Q water at concentrations up to 10 times that of the original stock. Additionally, we found that the residue was soluble in methanol, ethanol, and chloroform. However, the dye degraded (color faded and turned yellowish) within a week when a $CDCl_3$ solution of the dye was accidentally left in an

NMR tube at room temperature. A UV-Vis spectrum of the dye in Milli-Q water revealed an absorption maximum at 483 nm (Figure S5A). The dye solution was run through HPLC (Figure S5B), and a single peak was identified. Mass spectra of the aqueous solution of the dye were taken and a strong peak at m/z = 291.7 and a weaker peak at m/z = 582.2 were detected (Figure S5C). We assign the peak at m/z = 582.2 to be from [M^+] species and the peak at m/z = 291.7 to be from [$M+H^+$] species. We assume that there is at least one counter-anion permanently associated with the molecule and the molecular weight may range between approximately 620-660 Da. Given that 0.3 mg of dye residue was present in 0.5 mL solution, we estimate that the concentration of the stock solution of the dye is approximately 0.9-0.95 mM. The fluorescence turn-on behavior of QuantiFluor with RNA standard (0.33 ng/µL, Promega) was found to be practically unchanged between pH 7.4 and 5.1 (Figure S5D). QuantiFluor also did not display any fluorescence turn on when it was added to a dispersion of multilamellar vesicles having the same lipid composition as the target vesicles used in content transfer experiments (Figure S5E).

Control experiments for content transfer assay: At neutral pH (7.4) or at slightly acidic pH (6.4), we did not observe any fluorescence turn on events. We found that turn on events can be observed when a pH 5.1 buffer is flown, i.e. under the well-established condition known to cause influenza membrane fusion. Next, we carried out a control experiment to rule out any possibility that turn on events can be caused by QuantiFluor leaking out of a target vesicle and diffusing into a ruptured virus particle and binding to the vRNPs. We estimate that there are ~30 QuantiFluor molecules in a 100 nm target vesicle. If we assume that there are as high as 10^4 tethered vesicles per field of view (83 µm × 83 µm), and further assuming uniform coverage of the flow cell channel (2.5 mm × 1.3 mm × 0.07 mm) surface, the maximum concentration of QuantiFluor inside the flow cell will only be ~1 nM if all vesicles are ruptured and the dye is spread over the entire volume of the flow cell. To simulate an extreme condition (as discussed above) where all target vesicles ruptured and released the encapsulated QuantiFluor, we included 1.5 nM of QuantiFluor in the *fusion buffer* (pH 5.1). This buffer was flown to tethered target vesicles (lacking any QuantiFluor inside) bound to influenza virus particles. However, no turn on of QuantiFluor (due to binding to vRNPs in any ruptured virus particles) were observed (SI Video 2). This experiment establishes that the fluorescence turn on of QuantiFluor indeed takes place only when it diffuses from the target vesicles to the virus particle through the fusion pore and not due to rupture of virus or vesicle.

Analysis of content transfer kinetics data. In our methodology for analyzing video data, we employed a multi-faceted approach that primarily revolves around detecting and quantifying pixel intensity variations over time. Initially, the video frames were extracted from .tif files and subjected to preprocessing. This preprocessing involves using a 9×9 averaging filter to smooth pixel values, which significantly enhances the accuracy of our subsequent analyses. This step plays a crucial role in noise reduction, contributing to the improved fidelity of event detection. To further enhance the accuracy of our analysis, we excluded the 3 layers of pixels very close to the edges of the images, as any event occurring there may not be fully captured. Following the initial smoothing step, we implemented a multi-threshold strategy to identify substantial changes in pixel intensity across frames. These changes serve as indicators of events of interest. To further refine our data, we incorporated various filtering techniques. This includes the removal of redundant and adjacent pixel events to ensure the independence of detected events. Additionally, we applied a low-pass filter to smoothen the signal, facilitating the identification of more subtle changes in intensity. This was used later with the MATLAB function "findpeaks." By utilizing this function, we can determine the location of peak maxima, their prominence, and their width. Peaks that exceeded certain arbitrarily defined thresholds in terms of width and height were considered as fusion events. Once the events were detected, we calculated a

cumulative distribution function (CDF) of the wait times. The MATLAB codes are available at the following link: https://github.com/boxerlab/Content-Transfer.

Preparation and characterization of gel-phase supported lipid bilayer surface. A film was created by evaporating a 20 µL of 5 mg/mL chloroform solution of DPPC in a glass vial. The film was suspended by incubation with 200 µL *vesicle buffer* at 65 °C followed by vortexing. The multilamellar dispersion was extruded through 50 nm polycarbonate filter while keeping the extrusion block on a hot plate (65 °C). 20 µL of the extruded ULVs were taken and DNA-lipid conjugates (**L-dN$_{24}$1** and **L-dN$_{24}$2**) were added as shown in Figure 5A. The solution was kept at 65 °C for 30 min. A flow cell was freshly prepared by plasma cleaning and PDMS bonding and 10 µL of the warm DPPC ULVs incorporating two kinds of DNA-lipid conjugates were immediately added to the channels and the flow cell is left at room temperature for ~10 min. Mole fractions of the DNA-lipid conjugates were chosen with respect to DPPC such that there were approximately 4 DNA-lipid conjugates of each kind on average within a 100 nm×100 nm region of the SLB. After this, the channels were rinsed with 2 mL of *vesicle buffer*. After this, vesicles displaying appropriate complementary DNA-lipid conjugates were added to the flow cell and allowed to bind for ~10 min. The concentration of vesicles was such that there were approximately 500-600 vesicles per FOV and well-separated from one another. It is notable that in the absence of the DNA-lipid conjugates in either or both the SLB or vesicles, negligible (<10/FOV) binding of vesicles were observed. In order to test whether the DPPC SLBs had any major defects (micrometer-sized cracks, holes, etc), they were incubated with Texas Red-labeled bovine serum albumin (TR-BSA, Invitrogen). If defects were present, TR-BSA bound to the exposed glass surface at the defect sites and the corresponding fluorescence patterns could be imaged by microscope (Figure S16B-C). We thoroughly optimized the preparation technique such that we could consistently produce gel-phase SLBs free of major defects.

Dual labeling of influenza virus particles: At first membranes of influenza virus particles (corresponding to nominal protein concentration in the labeling mixture: 0.4 mg/mL) are labeled with Texas Red-DHPE by incubating the virus sample with 2.5 µM of Texas Red-DHPE in *vesicle buffer* at RT for 1 h. Next, 7 µL of *vesicle buffer* is added to 2 µL of Texas Red DHPE-labeled virus. 1 µL of QuantiFluor (~0.45 mM in *vesicle buffer*) is added to it and the tube is kept at RT for ~2 h to allow labeling of the internal vRNPs. A flow cell is freshly prepared and 1 µL of the dually labeled virus was further diluted with 7 µL *vesicle buffer* and added to allow it to adsorb to the cleaned glass surface. The unbound particles are removed by rinsing with *vesicle buffer* and imaging is performed subsequently.

Table S1. Summary of the fluorogenic nucleic acid-binding dyes screened in this study.

Dye	Supplier	MW (g mol^{-1})	λ_{em} (nm)	λ_{ex} (nm)	ε_{max} ($M^{-1}cm^{-1}$)	Content transfer assay
QuantiFluor®	Promega	582.2[a]	492	540	N.A	Yes
Thiazole Green (SYBR® Green I)	Biotium	509.73	498	522	58,000	Yes
SYBR™ Green II	Thermo Fisher	454.19	497	520	--	Yes
SYBR™ Safe	Thermo Fisher	504.66	502	530	--	No
Oxazole Gold (SYBR® Gold)	Biotium	495.66	496	539	57,000	Yes
EvaGreen®	Biotium	1119.06	500	530	35,000[c]	Yes
SYTO™ 11		~400	508/510	527/530		No
SYTO™ 12		~300	499/500	519/522		No
SYTO™ 13		~400	488/491	509/514		No
SYTO™ 14	Thermo Fisher[b]	~500	517/521	549/547	>50,000	No
SYTO™ 16		~450	488/494	518/525		No
SYTO™ 21		~500	494	517		No
SYTO™ 24		~550	490	515		No
SYTO™ 25		~450	521	556		No
DiYO™-1	AAT Bioquest	1270.65	491	508	98,900	Yes
ThT-NE	Sigma Aldrich	346.92	461	495	19,000[c]	No
Qubit™ RNA BR Reagent	Thermo Fisher	N.A.	644	673	N.A	No
Indolizine dye	(synthesized)[d]	362.21	556	608	27,500	No

[a] molecular ion peak detected by MS (Figure S5C); [b] sampler kit; [c] free dye in PBS, N.A. Not available. In the case of SYTO™ 11-16, the excitation/emission wavelengths correspond to dye bound to DNA/RNA; [d] reference 24. “Yes” and “No” in the extreme right column denote whether a particular dye is suitable for content transfer experiment or not.

Supplementary Figures

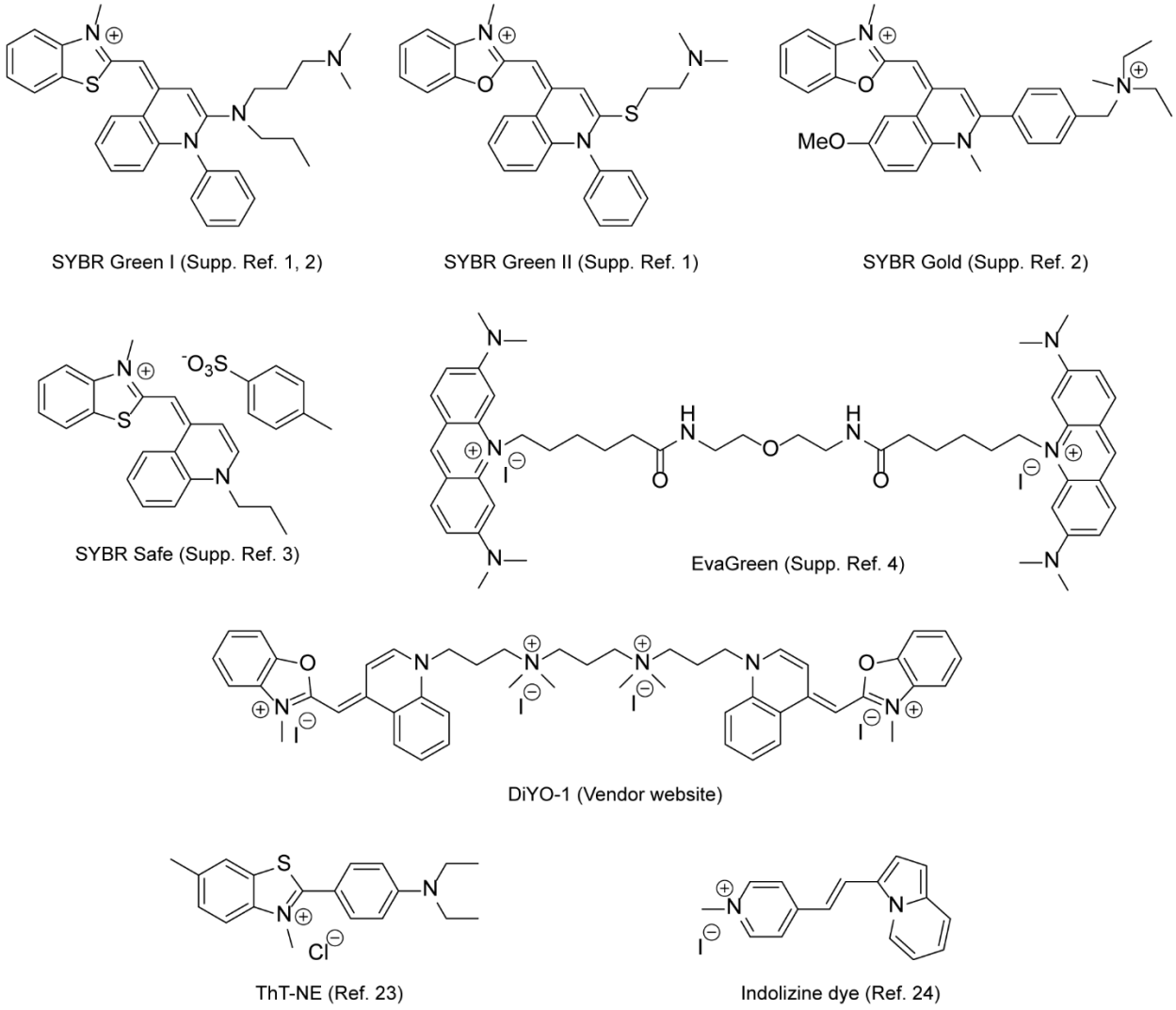

Figure S1. Dyes with known chemical structures used in this work. The structures were taken from indicated references in main text (Ref. 30, 31) or supplementary information (such as for SYBR Green I,[1,2] SYBR Green II,[1] SYBR Gold,[2] SYBR Safe,[3] EvaGreen[4]) or from website of commercial vendor.

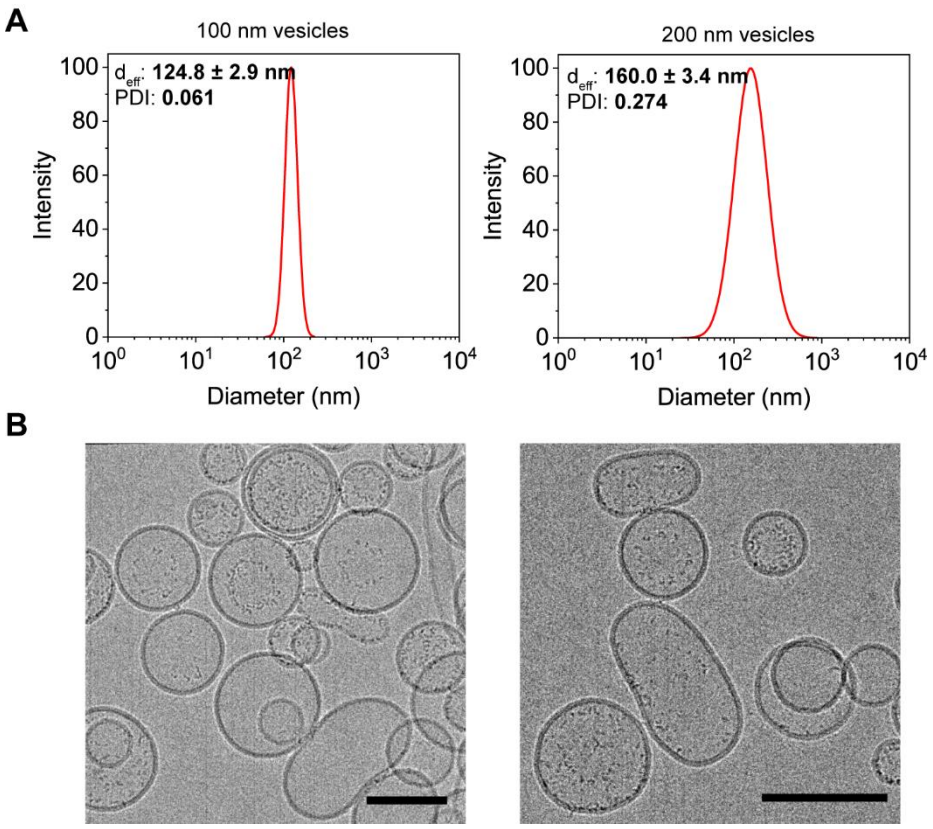

Figure S2. Preparation and characterization of unilamellar vesicles (ULV) used for viral fusion studies. **A**. Dynamic light scattering (DLS) characterization of extruded vesicles having compositions (37.5:20:40:2:0.5 POPC:DOPE:Cholesterol:GD1a:Biotin-DPPE) representative of what was used in viral fusion experiments. d_{eff}: effective diameter, PDI: polydispersity index. **B**. Cryogenic transmission electron microscopy images of 100 nm vesicles used for viral fusion experiments. Scale bars represent 100 nm.

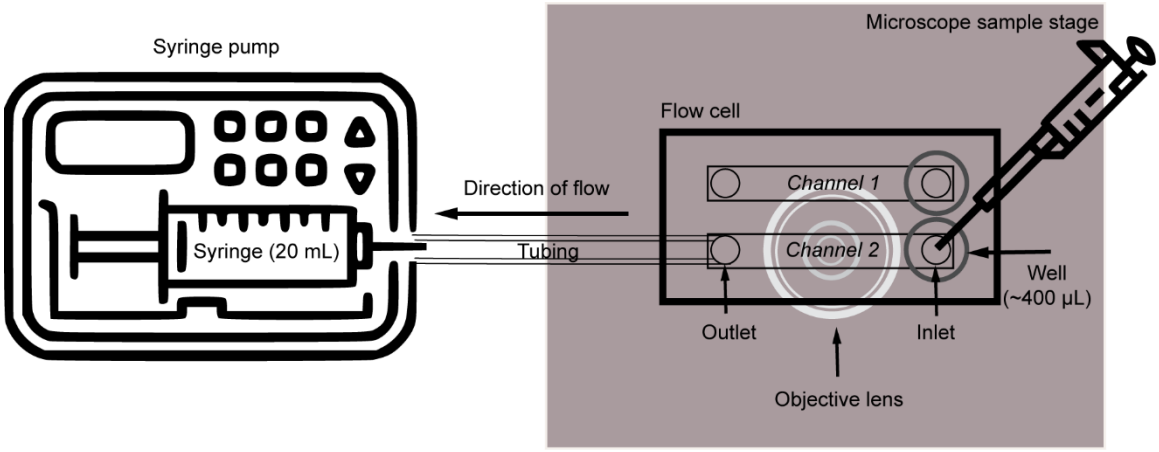

Figure S3. A schematic diagram (*top view*) of the experimental setup used for viral fusion experiments on a microfluidic flow cell. Vesicles and viruses are tethered inside the channels (1 and/or 2).

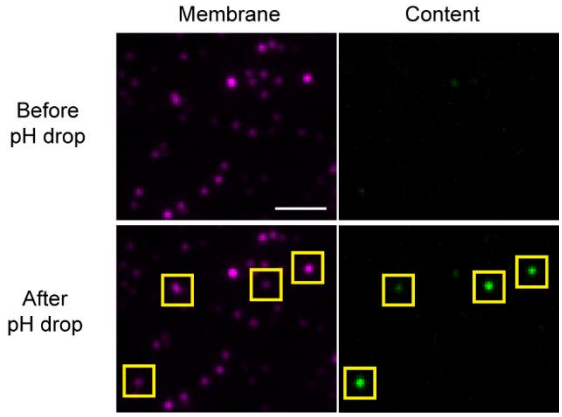

Figure S4. Screening of nucleic-acid binding dyes capable of binding to viral ribonucleoprotein (vRNP) complexes. In a typical screening experiment, vesicles stained with Texas Red-DHPE and encapsulating a nucleic acid-binding dye were imaged by excitation with 561 nm (membrane: *magenta*) and 488 nm (content: *green*) light before and after pH drop (i.e., 7.4 → 5.1). Appearance of a new green spot co-localizing with a magenta spot (marked in yellow squares) indicated that the dye was capable of binding to vRNPs upon membrane fusion. Scale bar: 3 μm.

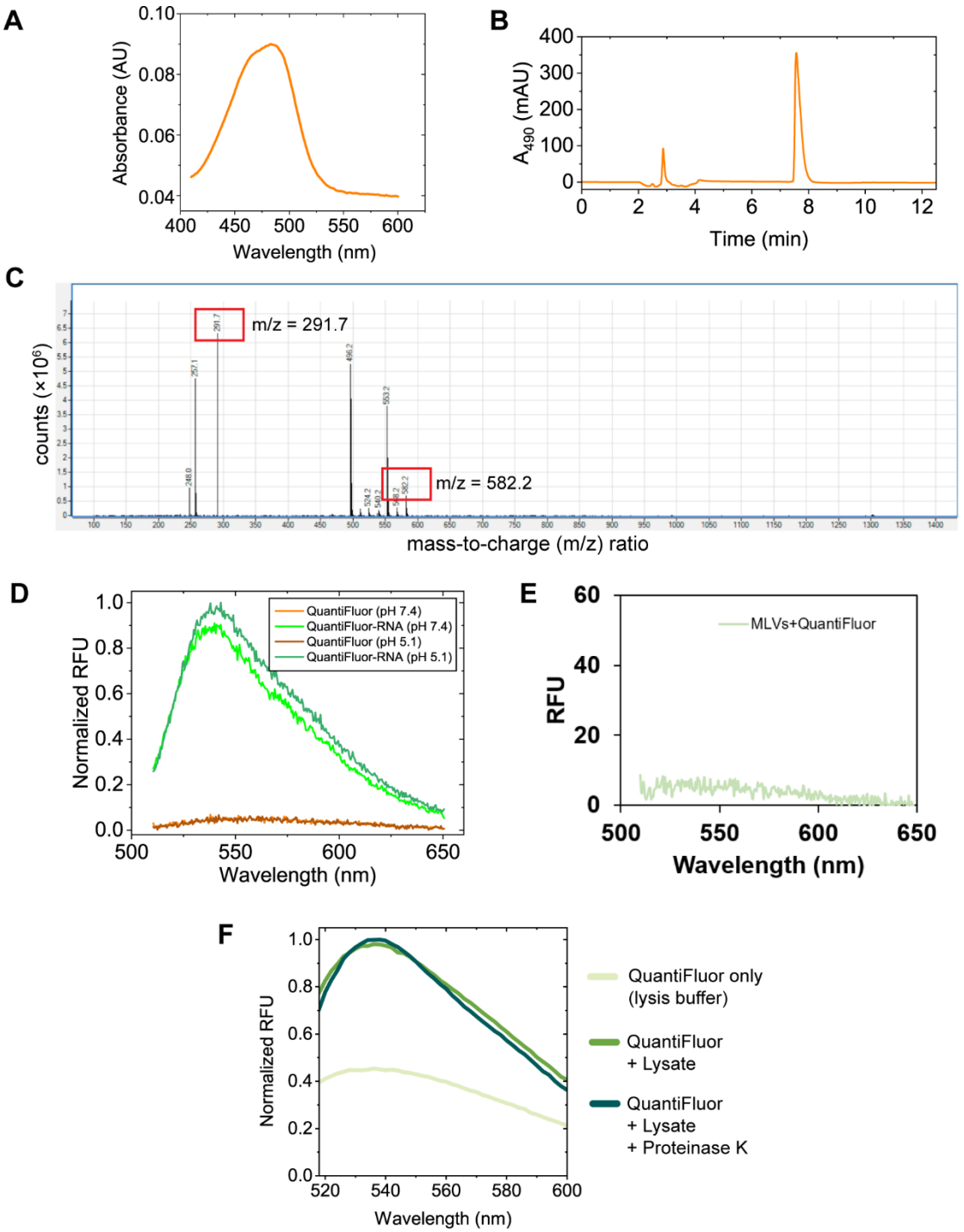

Figure S5. Characterization of QuantiFluor. **A**. Absorption spectrum of a solution of the dye in Milli-Q water. **B**. HPLC chromatogram (490 nm detection, 4 mL/min flow rate) of QuantiFluor dissolved in Milli-Q water injected into a Zorbax C18 semi-quantitative column. The small peak at 3 min is likely not a real analyte peak – rather an artifact often observed at void volume of the column. **C**. ESI-MS analysis of an aqueous solution of QuantiFluor on Agilent Triple Quadrupole instrument (positive mode). **D**. QuantiFluor shows negligible fluorescence at pH 7.4 (*vesicle buffer*) or pH 5.1 (*fusion buffer*). The fluorescence increases significantly in the presence of an RNA standard (0.33 ng/µL, Promega) either at pH 7.4 or 5.1. The fluorescence enhancement

upon binding to RNA is very similar at these pH values. Excitation wavelength: 492 nm, scan range: 510-650 nm. **E**. QuantiFluor shows negligible fluorescence when added to a dispersion of multilamellar vesicles (MLVs). **F**. Fluorescence emission spectra of QuantiFluor (approximate concentration: 10 µM) added to influenza viral lysate shows significant turn on as compared to dye only.

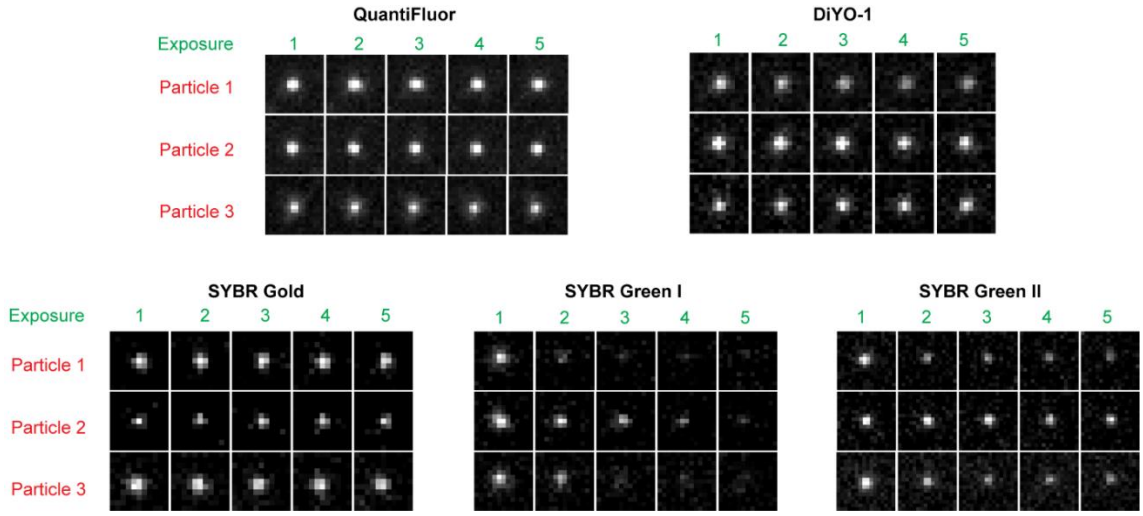

Figure S6. A semi-qualitative comparison of the photostability of various nucleic acid-binding dyes screened for content transfer experiments. Each fluorescent spot (3 representative spots shown for each dye) that represents a fusion event was exposed 5 consecutive times with same illumination intensity and time and images were taken. All images were window-leveled in the identical manner. It can be seen that SYBR Green I has the most inferior apparent photostability as judged from the near-disappearance of the spots by the 4th exposure.

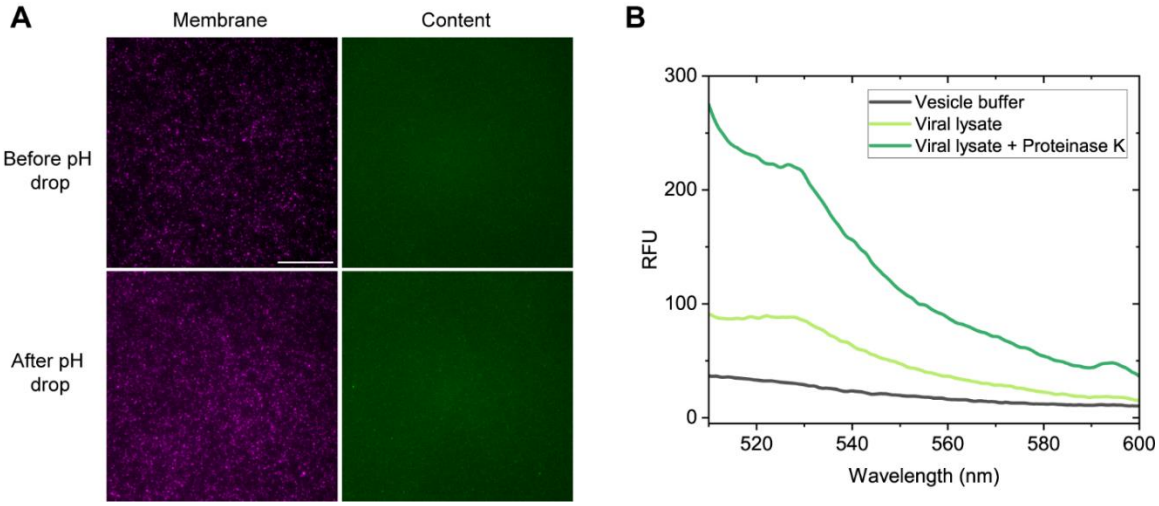

Figure S7. Test of EvaGreen as a content transfer assay dye. **A**. Vesicles encapsulating EvaGreen were imaged before and after fusion and no "successful" content transfer events were detected as judged from the signals in the "Content" channel. **B**. EvaGreen showed negligible fluorescence in *lysis buffer*. A small increase in fluorescence was observed in presence of lysed virus sample while a significantly larger fluorescence was observed when the lysate was digested with Proteinase K – suggesting that EvaGreen cannot possibly efficiently bind to viral RNA when it is complexed with nucleoproteins.

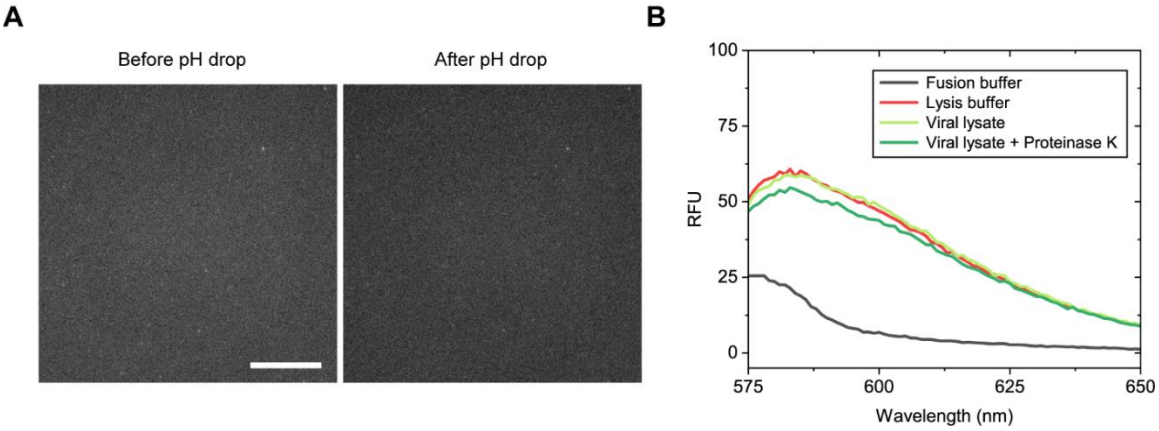

Figure S8. Test of an indolizine dye as a content transfer assay dye. **A**. 100 nm vesicles (37.4:20:40:2:0.5:0.1 POPC: DOPE: Cholesterol: GD1a: Biotin-DPPE: Atto 647N-DMPE) encapsulating the indolizine dye (*E*)-4-(2-(indolizin-3-yl)vinyl)-1-methylpyridinium iodide[5] did not display any fluorescence turn on events after pH drop (7.4 → 5.1) when viruses were added. Scale bar: 20 µm. **B**. When the dye is added to a viral lysate, no significant fluorescence enhancement is detected as compared to the fluorescence of the dye in *lysis buffer* only.

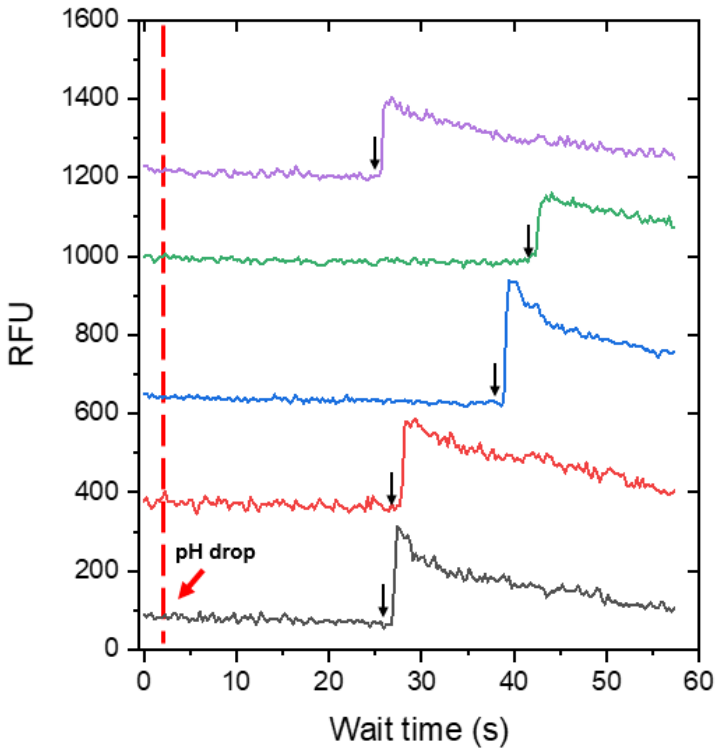

Figure S9. Representative fluorescence intensity traces (from continuous video stream recording a single experiment) corresponding to individual fusion events between influenza virus particles and 100 nm vesicles encapsulating QuantiFluor. After a certain wait-time (indicated by black arrows), a sudden spike in the fluorescence signal takes place when the vRNPs bind to QuantiFluor upon fusion. The signal gradually decays due to photobleaching.

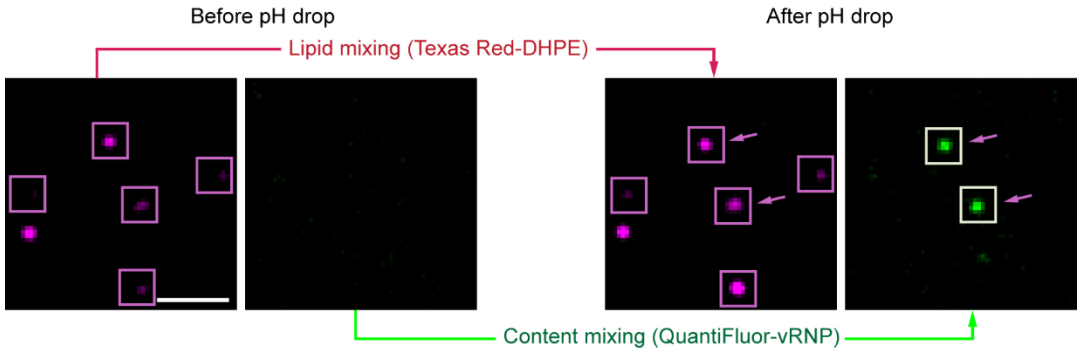

Figure S10. Images of 100 nm vesicles undergoing lipid mixing and content transfer (marked in square boxes) upon fusion with influenza virus. During lipid mixing event, the signal in membrane channel (*magenta*) turned brighter while during content transfer, a new spot appeared in the content channel (*green*) due to fluorescence turn-on. The arrows indicate the virus-vesicle pairs undergoing simultaneous lipid mixing and content transfer. Scale bar: 10 μm.

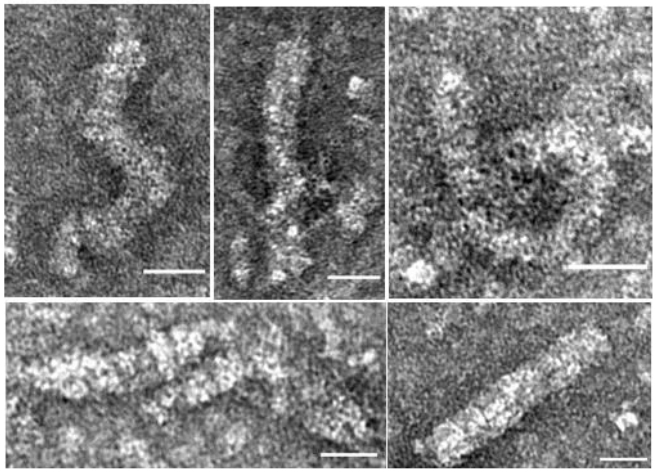

Figure S11. Negative-staining transmission electron microscopy (TEM) images of viral ribonucleoprotein (vRNP) complexes obtained upon lysis of virus particles. The morphologies of vRNPs are consistent with previous electron microscopy observations.[6–8] All scale bars denote 25 nm. The images illustrate that the vRNPs are well-ordered macromolecular complexes tens of nm in length. Therefore, it is apparent that for vRNPs to freely distribute within the fusion volume, the fusion pore must be several tens of nm in width too.

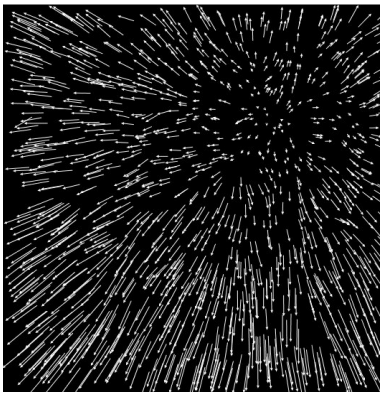

Figure S12. A distortion map of chromatic aberration across the entire FOV (83 μm×83 μm) of the objective lens (Nikon Apo TIRF, NA = 1.49, 100X) used for all imaging experiments. The arrows indicate displacement vectors corresponding to chromatic shift direction from *magenta* (561 nm) channel to *green* (488 nm) channel directions. The lengths of the vectors are exaggerated (by multiplying each displacement vector by $50/r_{max}$, where r_{max} = longest displacement vector) for clearer visual representation (Reference 32 in main text).

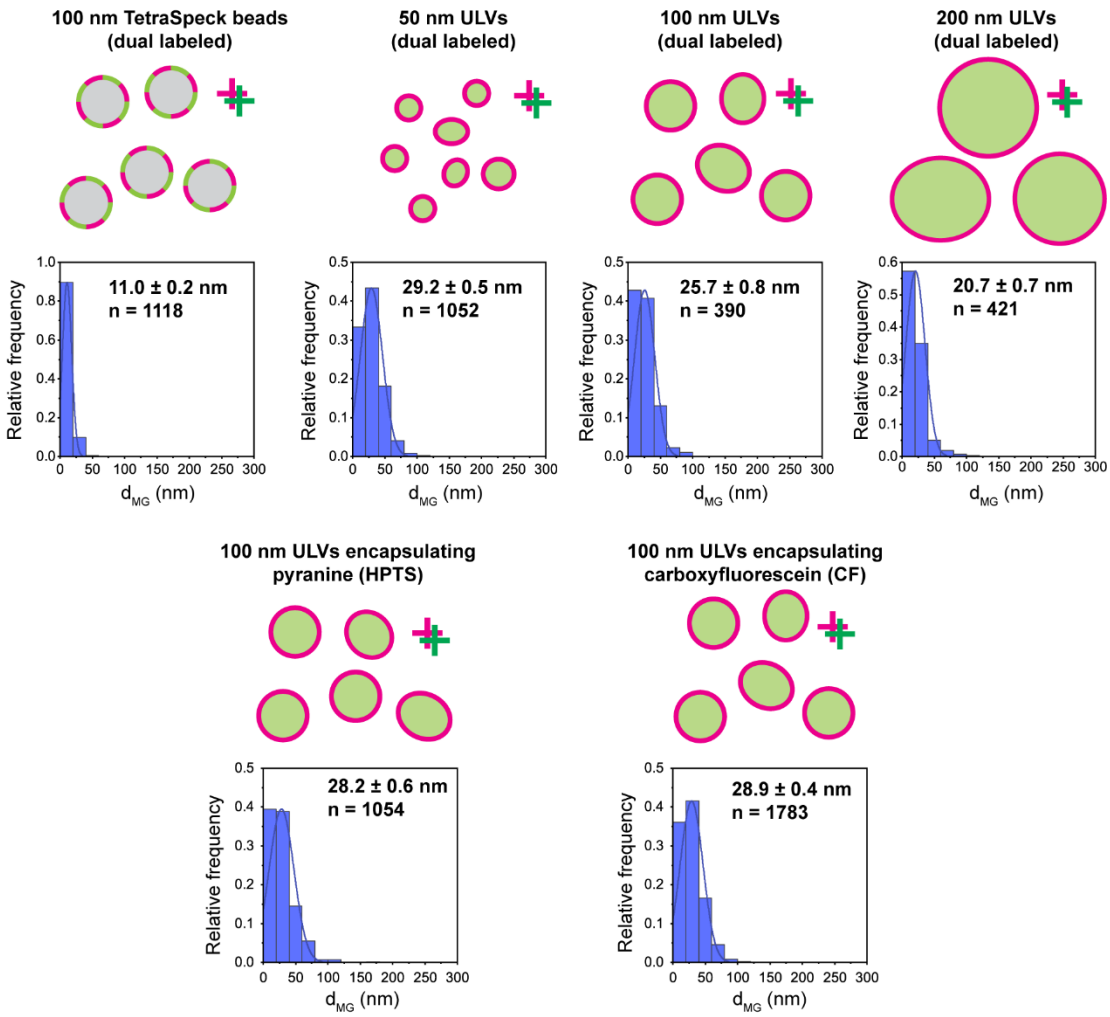

Figure S13. Distribution of d_{MG}'s for several dually labeled particles. The magenta and green colored '+' signs adjoining the schematics are used to denote that the centroids in corresponding channels are expected to overlap. Data was binned into 20 nm intervals for all distributions. All error values denote standard error.

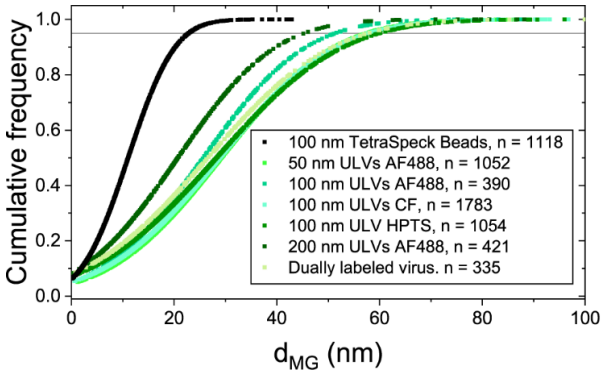

Object	$d_{MG, mean}$ (nm)	$d_{MG, cut-off}$ (nm)
100 nm TetraSpeck Beads	11.0 ± 0.2	22.9
50 nm ULVs (AF488)	29.2 ± 0.5	57.5
100 nm ULVs (AF488)	25.7 ± 0.8	51.2
100 nm ULVs (CF)	28.9 ± 0.4	58.0
100 nm ULVs (HPTS)	28.2 ± 0.6	59.9
200 nm ULVs (AF488)	20.7 ± 0.7	45.5
Dually labeled virus	28.6 ± 1.0	57.6

Figure S14. Cumulative distribution functions of Euclidean distances between centroids of *magenta* (membrane) and *green* (content) signals (d_{MG}) from objects where the signals fully overlap. The corresponding histograms are shown in Figures 4C and S13. $d_{MG, mean}$ represents the mean of the distribution of distances and the error represents standard error. $d_{MG, cut-off}$ represents the value below which 95% of the distances lie. The row for dually labeled virus is marked in a red box.

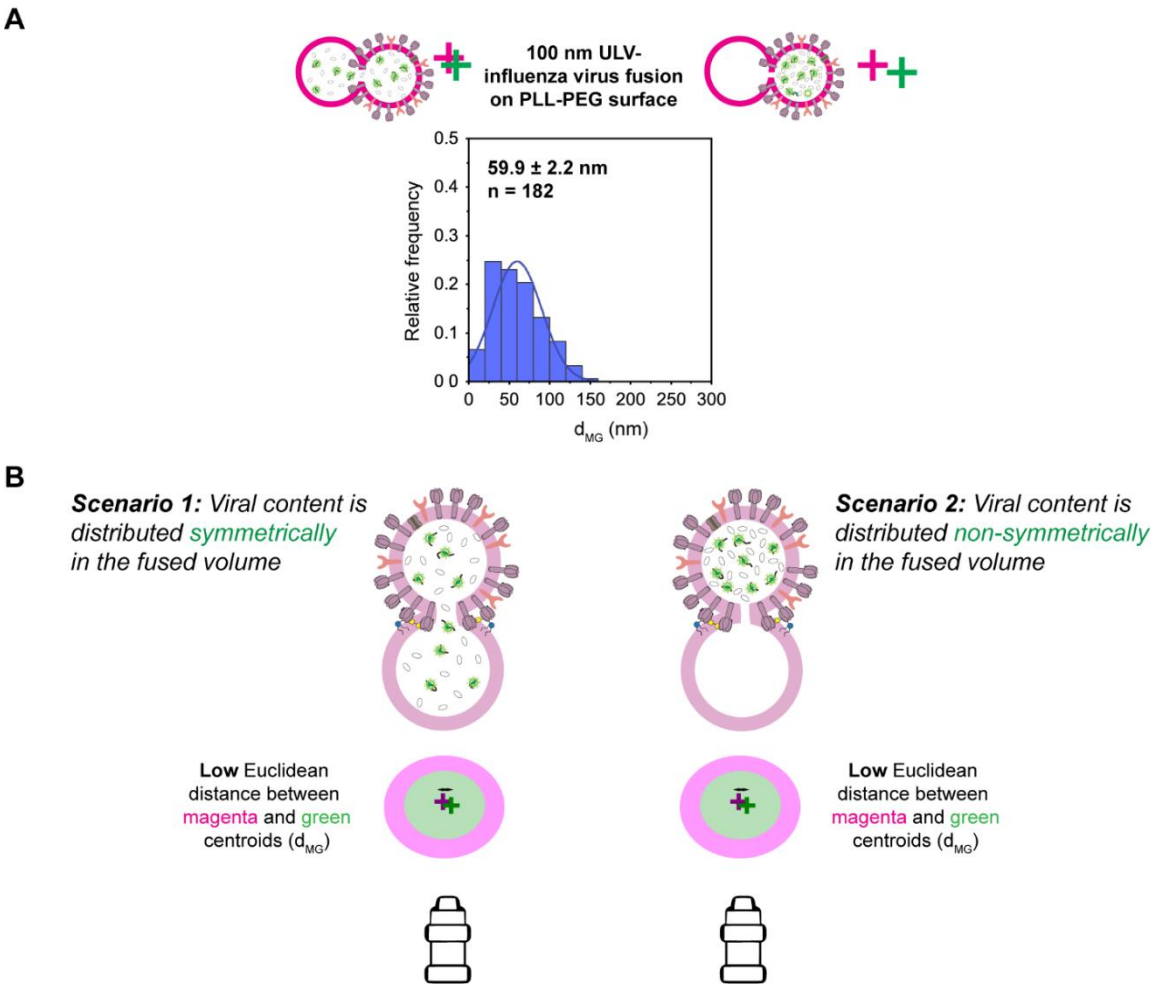

Figure S15. **A**. Distribution of Euclidean distances between the centroids of sub-diffraction spots in *magenta* and *green* channels (d_{MG}) corresponding to fusion of 100 nm unilamellar vesicles tethered to PLL-PEG surface with influenza virus in a configuration as depicted in Figure 1B. The data were binned to 20 nm intervals. Error value indicates standard error. **B**. Schematic diagram showing fusion of influenza virus to polar regions of the target vesicles. In such events, no distinction can be made between super-localization microscopy between *Scenario 1*: viral content is distributed non-symmetrically in the fused volume; *Scenario 2*: viral content is distributed non-symmetrically in the fused volume.

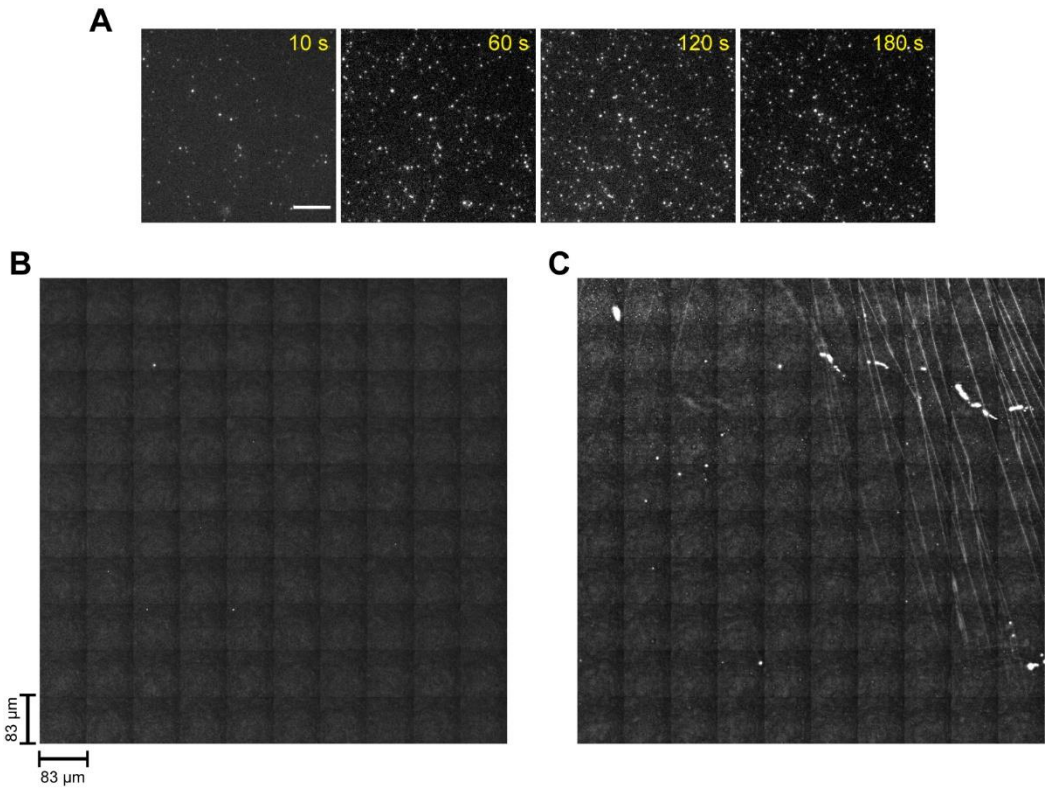

Figure S16. Gel-phase supported lipid bilayers (SLB) as a functionalizable platform for carrying out viral fusion experiments. **A**. Time-lapse images of binding of 100 nm vesicles to DPPC SLBs via interaction between complementary DNA-lipid conjugates inserted into the vesicles and the SLB. Scale bar: 20 µm. **B**. A montage of 10×10 contiguous image tiles (each 83 µm×83 µm) of DPPC SLBs treated with TR-BSA showing lack of any micrometer-sized defects. **C**. A montage of 10×10 contiguous image tiles (each 83 µm×83 µm) of DPPC SLBs treated with TR-BSA showing large defects in the form of cracks and voids. It is notable that this SLB was deliberately prepared in a manner that such defects were introduced. In this case, the DPPC ULV solution was added to the plasma cleaned glass slide when it was nearly at room temperature instead of adding it when it is at 65 °C.

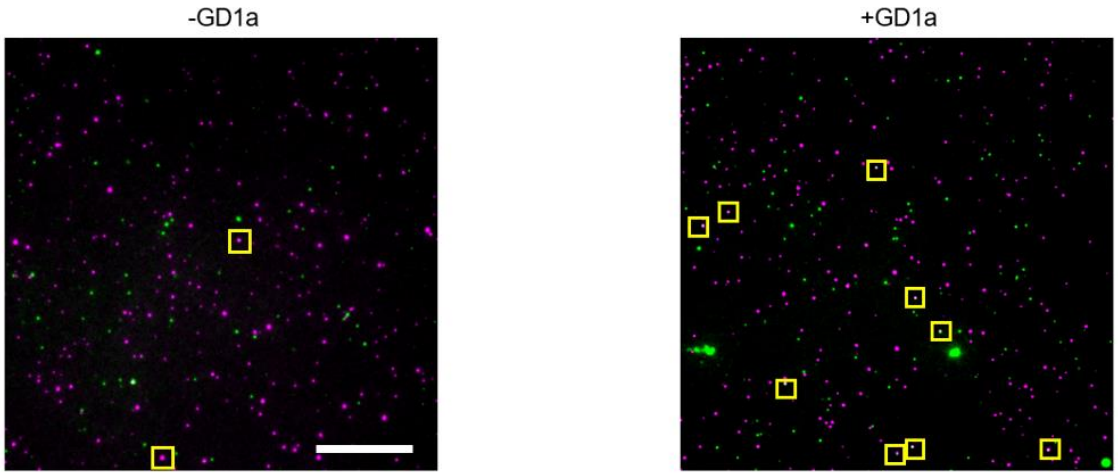

Figure S17. Side-by-side tethering of viruses and vesicles on gel-phase (DPPC) supported lipid bilayer (SLB) is a low probability event.100 nm vesicles (*magenta* spots) lacking (-GD1a) or containing (+GD1a) GD1a in their membranes and influenza virus particles internally labeled with QuantiFluor (*green* spots) were sequentially tethered to DPPC SLBs via two sets of complementary DNA-lipid conjugates as illustrated in Figure 5A. When the vesicles lack any GD1a chance association of a virus and vesicle is extremely low (10 in 1000). When the vesicles contain GD1a, the chance of association is significantly higher (43 in 1000). The virus particles co-localizing with vesicles are marked in square boxes. Data were analyzed using ThunderSTORM plugin of FIJI. Scale bar represents 20 µm.

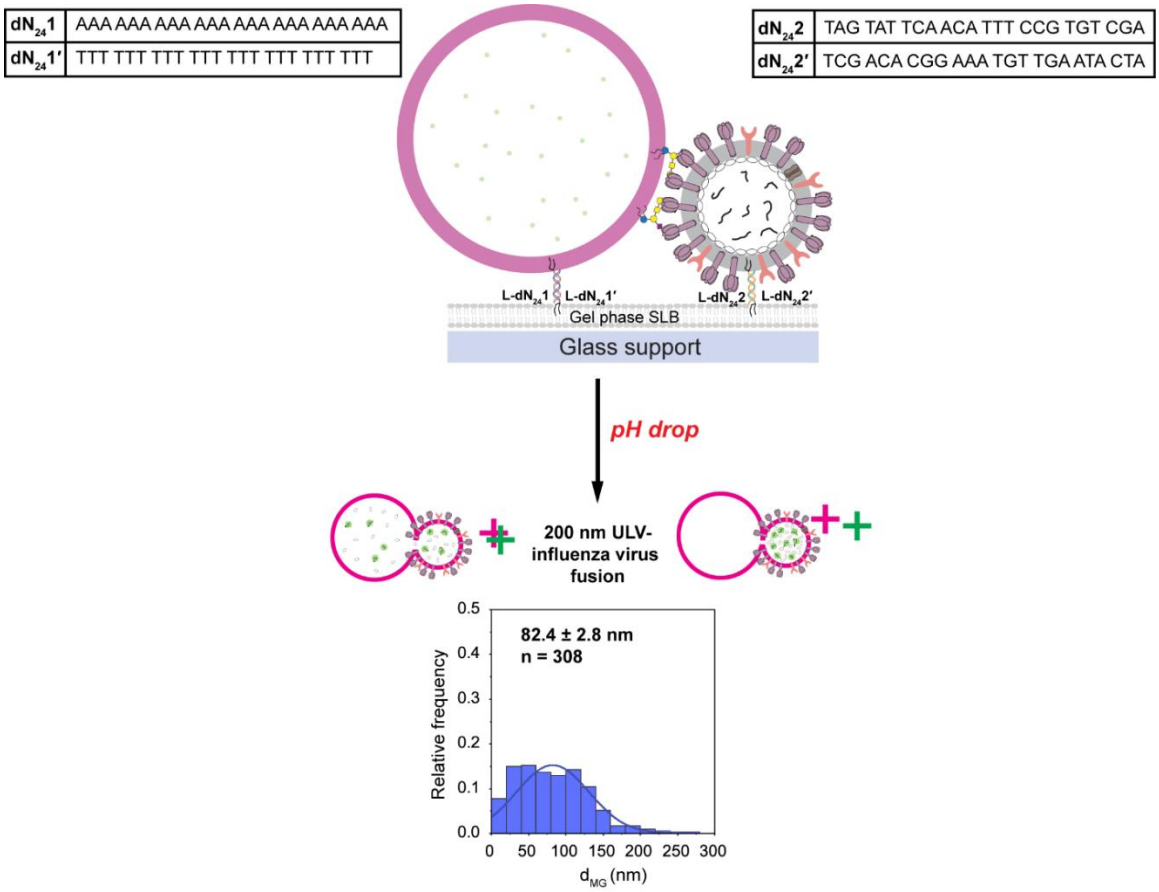

Figure S18. Distribution of Euclidean distances between the centroids of sub-diffraction spots in *magenta* and *green* channels (d_{MG}) for 200 nm unilamellar vesicles fused with influenza virus on gel-phase (DPPC) SLB surface. The data were binned to 20 nm intervals. Error value indicates standard error.

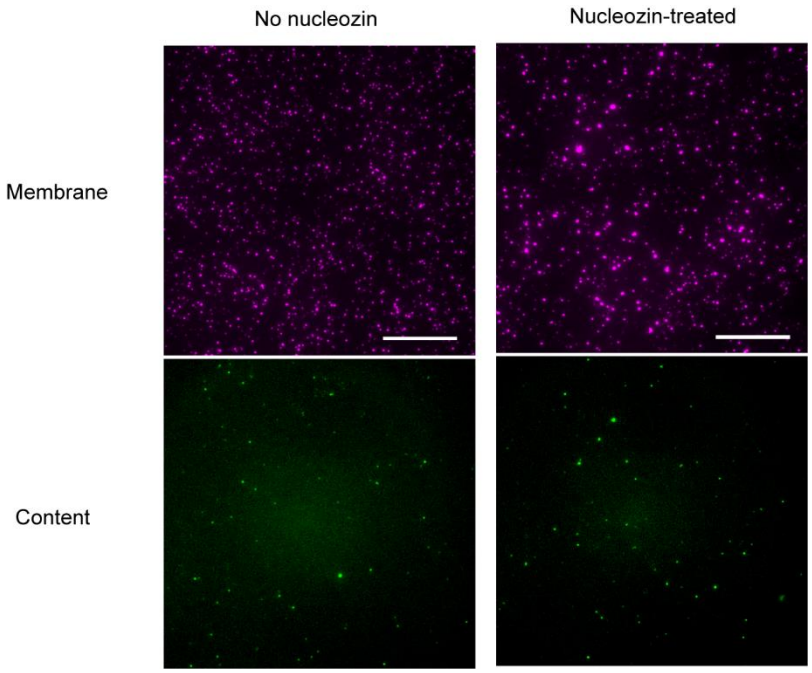

Figure S19. Representative fluorescence micrographs correspond to the outcome of fusion of target vesicles (encapsulating QuantiFluor) with influenza virus particles *untreated* (No nucleozin) or treated (Nucleozin-treated) with nucleozin. Scale bars correspond to 20 µm.

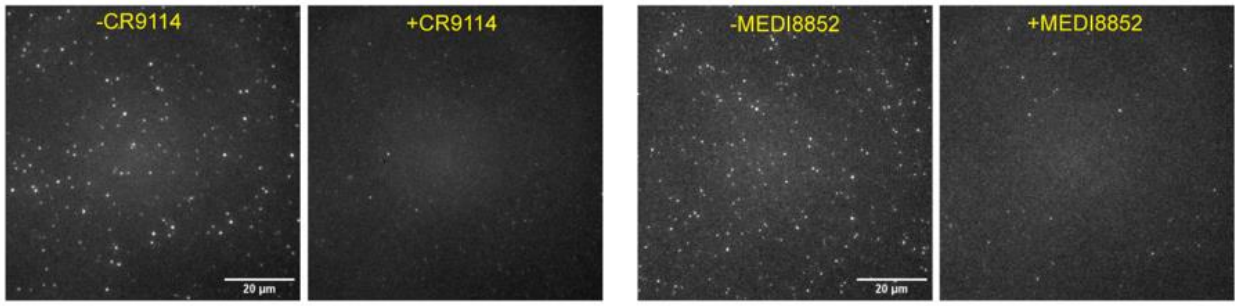

Figure S20. Cell-free assessment of inhibitory effects of broadly neutralizing antibodies on viral fusion. When influenza virus particles (0.2 mg/mL protein) were incubated with neutralizing antibodies CR9114 (4 µM) and MEDI8852 (4 µM) for 24 h at 4 °C, 91% and 88% reduction in the fusion events are observed respectively. Scale bars: 20 µm.

Supplementary Video Captions

SI Video 1: A time-lapse video in 488 nm channel from a representative fluorogenic content transfer assay experiment. 100 nm unilamellar vesicles (membrane labeled with Texas Red-DHPE and encapsulating QuantiFluor) were tethered to a passivated glass surface and influenza virus particles were bound to the vesicles. Virus-vesicle fusion was induced by flowing in pH 5.1 buffer. Fluorescent spots can be seen appearing corresponding to individual fusion event. Scale bar represents 15 µm and the duration of the video is 60 s.

SI Video 2: A time-lapse video in 488 nm channel from a control experiment for content transfer assay experiment. 100 nm unilamellar vesicles (membrane labeled with Texas Red-DHPE) were tethered to a passivated glass surface and influenza virus particles were bound to the vesicles. pH 5.1 buffer containing 1.5 nM QuantiFluor was flown to induce fusion and also to check whether externally added QuantiFluor can cause fluorescence turn on. Scale bar represents 15 µm and the duration of the video is 60 s.

Supplementary References

(1) Saarnio, V. K.; Salorinne, K.; Ruokolainen, V. P.; Nilsson, J. R.; Tero, T. R.; Oikarinen, S.; Wilhelmsson, L. M.; Lahtinen, T. M.; Marjomäki, V. S. Development of Functionalized SYBR Green II Related Cyanine Dyes for Viral RNA Detection. *Dye. Pigment.* **2020**, *177*, 108282.

(2) Kolbeck, P. J.; Vanderlinden, W.; Gemmecker, G.; Gebhardt, C.; Lehmann, M.; Lak, A.; Nicolaus, T.; Cordes, T.; Lipfert, J. Molecular Structure, DNA Binding Mode, Photophysical Properties and Recommendations for Use of SYBR Gold. *Nucleic Acids Res.* **2021**, *49* (9), 5143–5158.

(3) Evenson, W. E.; Boden, L. M.; Muzikar, K. A.; Oleary, D. J. 1H and 13C NMR Assignments for the Cyanine Dyes SYBR Safe and Thiazole Orange. *J. Org. Chem.* **2012**, *77* (23), 10967–10971.

(4) Shoute, L. C. T.; Loppnow, G. R. Characterization of the Binding Interactions between EvaGreen Dye and DsDNA. *Phys. Chem. Chem. Phys.* **2018**, *20* (7), 4772–4780.

(5) Kim, M. J.; Li, Y.; Junge, J. A.; Kim, N. K.; Fraser, S. E.; Zhang, C. Development of Highly Fluorogenic Styrene Probes for Visualizing RNA in Live Cells. *ACS Chem. Biol.* **2023**, *18* (7), 1523–1533.

(6) Arranz, R.; Coloma, R.; Chichón, F. J.; Conesa, J. J.; Carrascosa, J. L.; Valpuesta, J. M.; Ortín, J.; Martín-Benito, J. The Structure of Native Influenza Virion Ribonucleoproteins. *Science* **2012**, *338* (6114), 1634–1637.

(7) Coloma, R.; Arranz, R.; Rosa-trevín, J. M. De; Sorzano, C. O. S.; Munier, S.; Carlero, D.; Naffakh, N.; Ortín, J.; Martín-benito, J. Proteins Reveal a Processive Helical Track as Transcription Mechanism. *Nat. Microbiol.* **2020**, *5* (May), 727–734.

(8) Moeller, A.; Kirchdoerfer, R. N.; Potter, C. S.; Carragher, B.; Wilson, I. A. Organization of the Influenza Virus Replication Machinery. *Science* **2012**, *338* (6114), 1631–1634.